UCLA
UCLA Previously Published Works

Title

MHz laser absorption spectroscopy via diplexed RF modulation for pressure, temperature, and species in rotating detonation rocket flows

Authors

Nair, Anil P
Lee, Daniel D
Pineda, Daniel I
et al.

Check for updates

MHz laser absorption spectroscopy via diplexed RF modulation for pressure, temperature, and species in rotating detonation rocket flows

Anil P. Nair[1] · Daniel D. Lee[1] · Daniel I. Pineda[1] · Jason Kriesel[2] · William A. Hargus Jr.[3] · John W. Bennewitz[3] · Stephen A. Danczyk[3] · R. Mitchell Spearrin[1]

Abstract

A mid-infrared laser absorption sensing method has been developed to quantify gas properties (temperature, pressure, and species density) at MHz measurement rates, with application to annular rotating detonation rocket flows. Bias-tee circuitry is integrated with distributed feedback quantum cascade and interband cascade lasers in the $4-5$ μm range enabling diplexed radio frequency (RF) wavelength modulation on the order of several MHz while yielding sufficient scan depth to capture multiple rovibrational transitions in the fundamental vibrational bands of CO and CO_2. Sub-microsecond spectrally-resolved CO absorption lineshapes provide for inference of temperature and species from a two-line area ratio and pressure from collision line-width. CO_2 column density is inferred from peak-to-valley differential absorption at the bandhead near 4.19 μm. A field demonstration on a methane-oxygen rotating detonation rocket engine was performed utilizing an in situ single-ended retro-reflection optical configuration aligned at the exhaust plane. The target gas properties are temporally-resolved at up to 3 MHz across rotating detonations with up to 20 kHz cycle frequency.

1 Introduction

Propellant efficiency (i.e. specific-impulse) is of utmost importance in rocket propulsion systems due to the very high propellant mass fractions of launch vehicles. Detonation-based combustion (pressure-gain combustion) has gained interest for rocket propulsion applications due to theoretical thermodynamic advantages (compared to traditional deflagration-based combustion) which give potential for propulsion system mass reduction [1, 2]. Lower entropy production across detonation waves allows for a relative increase in post-reaction pressure and temperature [3], which may be used to (1) accelerate the combustion products to a higher

exhaust velocity (higher specific-impulse); (2) reduce the upstream feed pressure requirement on the system; and/or (3) reduce the downstream nozzle requirement to achieve similar specific-impulse. The short spatial scales involved in detonation combustion may also reduce combustion chamber size. Unfortunately, the dynamic unsteady nature of detonations and extreme range of thermodynamic conditions covered across very short temporal and spatial scales have made engine architectures challenging to model, design and control [4], slowing technical maturity and realization of theoretical benefits.

In recent years, rotating detonation engines (RDEs) have been the subject of considerable research and development effort as a potential engine architecture that best reconciles the practical challenges of detonation combustion [4–12]. In RDEs, propellant is fed steadily into an annular combustion chamber and consumed by a transverse detonation wave which continuously propagates (or rotates) around the annulus. This rotating detonation engine configuration is attractive in that it removes the need for high-frequency valve operation and unsteady thrust associated with linear pulse detonation engines (PDEs), but other challenges including mixing, injector backflow, and thermal management remain hurdles to development [13–16]. Notably, a critical issue in

✉ Anil P. Nair
   anilnair1995@g.ucla.edu

1   Department of Mechanical and Aerospace Engineering, University of California, Los Angeles (UCLA), Los Angeles, CA 90095, USA

2   Opto-Knowledge Systems, Inc. (OKSI), Torrance, CA 90502, USA

3   U.S. Air Force Research Laboratory, Edwards Air Force Base, CA 93524, USA

evaluating RDE technology has been a lack of diagnostic capability that is sufficiently quantitative and granular to provide useful feedback. In this work, we address this need by advancing the state-of-the-art in high-speed laser diagnostics for harsh combustion environments.

Quantitative laser diagnostic methods can provide means to interrogate flow-field properties in situ and elucidate combustion physics as well as propulsion system performance. Specifically, laser absorption spectroscopy (LAS) has shown considerable promise for quantifying temperature and species in detonation environments [17–22]. A persistent challenge to deploying LAS to detonation engines has been balancing the need for very fast measurement rates (to resolve steep property gradients) and the desire for robust methods for reliable quantitative data interpretation in such a harsh environment. Early LAS efforts on PDEs deployed fixed-wavelength laser absorption methods to probe hydrocarbon fuels [23, 24] and water vapor [21]. While fixed-wavelength absorption techniques are typically only limited in measurement rate by detector bandwidth, the methods are generally not robust against beam steering, particle scattering, window fouling, and thermal emission which are common and highly dynamic in detonation engines, and pronounced in rocket combustors [25]. To address these issues, more recent LAS work in the context of detonation engines has focused on wavelength-scanning or wavelength-modulation techniques that allow for reliable correction of thermal emission and active recovery of a non-absorbing baseline signal (or insensitivity to baseline signal) that mitigates issues of steering, scattering, and window fouling. Wavelength-scanning (or -modulating) spectroscopy techniques have been utilized for more robust PDE/RDE measurements of water vapor absorption in the near-infrared [18, 22, 26, 27] and the carbon oxides in the mid-wave infrared [17, 19, 20, 28]. However, the effective measurement rates for these wavelength scanning methods (10–100 kHz) are insufficient to fully resolve thermophysical gradients in many detonation-based engines. Specifically, rotating detonation rocket engines often possess cycle frequencies (which may involve multiple waves) in the range of 5–30 kHz, for which $\geq$ MHz measurement rate is desired for temporal resolution of intra-cycle transients.

In this paper, we present a mid-infrared laser absorption sensing method enabling MHz measurements of temperature, pressure and two major combustion species (CO and CO_2) in the annular exhaust flow of a rotating detonation rocket engine (RDRE). We first discuss the opto-electronic sensor design that enables radio-frequency (RF) wavelength modulation at MHz rates with mid-infrared sources. This is followed by details of the spectroscopic methods used to infer temperature, pressure, and species density from absorption spectra. We then describe the experimental setup involving a rotating detonation rocket test rig at the U.S. Air Force

Research Laboratory (in Edwards, CA USA), including a retro-reflection optical configuration. Demonstration results are shown and discussed, with a corresponding analysis of uncertainties.

2 Opto-electronic design

A key enabling element of this work is the integration of bias-tee circuitry with distributed feedback (DFB) quantum cascade and interband cascade lasers to facilitate RF wavelength modulation (or scanning). Bias-tees are diplexers which combine a constant electromagnetic signal, such as a direct laser injection current (DC), with a modulated signal or alternating current (AC). The ideal bias-tee consists of an inductor which admits DC signal (the bias) but blocks AC signals, teed with a capacitor which admits AC signals while blocking DC signals. The maximum modulation frequency is limited by the parasitic elements inherent to circuit components (e.g. the parasitic inductance in the capacitor).

For typical DFB laser control and modulation, a laser driver is used which stabilizes injection current and temperature with a closed-loop circuit. In these drivers, modulation is typically achieved by varying the laser set-point current. Modulation bandwidth is usually limited by the phase error or lag introduced by the various elements in the circuit, some of which are used for current stabilization, as well as preventing reverse bias or exceeding prescribed current limits. Bandwidth can be increased by using faster or fewer circuit elements, such as to minimize the phase error. However, given that commercial laser drivers are designed and built to minimize the risk of instability over a wide range of loads, the phase error resulting from the components used to achieve this stability results in a lower bandwidth than might be achieved by the laser. For quantum cascade lasers, injection current controllers with current range on the order of 1 Amp have typical modulation bandwidths on the order of 10^5 Hz [29], lower than can be achieved with diode laser controllers [30].

Approaching bandwidth limits renders an attenuation in the current modulation intensity and diminishing wavelength modulation. To circumvent this limitation, we integrate a bias-tee into the laser control circuit, using the conventional laser driver to set the bias or mean direct current (prescribing the center wavelength), while diplexing a radio frequency (RF) alternating current between the driver and laser. This effectively bypasses many circuit elements in the driver that constrain modulation bandwidth, but adds some risk of laser damage. Bias-tee circuits have been implemented (with commercial packaging) for near-infrared diode lasers [31], and have more recently been demonstrated with DFB quantum cascade lasers [32]. We note that this approach to
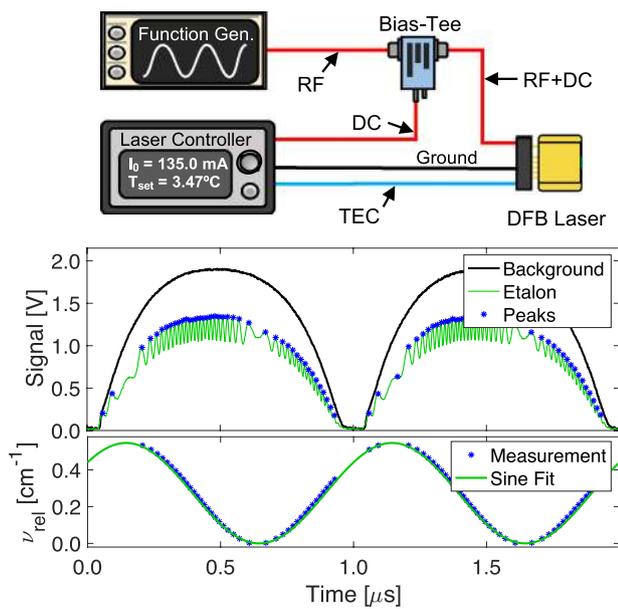
Fig. 1 Bias-tee laser control schematic (top). Sample MHz laser scans showing background and etalon scans (middle). Plot of resulting relative wavenumber vs. time calculated from the etalon peaks with sinusoidal fit (bottom)

rapid wavelength tuning is an alternative to laser pulsing, which can achieve similar rates, but has been observed to increase intensity noise and lower periodic stability [33, 34].

In this work, a continuous-wave distributed-feedback (DFB) quantum cascade laser (QCL) (ALPES Lasers), tunable from 2001 to 2012 cm^{-1}, and an interband cascade laser (ICL) (Nanoplus), tunable from 2382 to 2389 cm^{-1}, were used as the narrow-band light sources to probe rovibrational transitions of CO and CO_2 respectively. Both light sources were modulated using bias-tee circuitry as shown in Fig. 1. To avoid the 200 kHz bandwidth limitation of the laser controllers (Arroyo 6310-QCL and Arroyo 6305), the controllers are used solely to set the mean injection current, or DC bias, going into the laser and to control the temperature of the laser chip using thermoelectric cooling (TEC). Sinusoidal radio frequency current modulation is supplied by function generators (SRS DS345).

The direct current (DC) and alternating current (RF) signals are combined using commercial bias-tee diplexers (SigaTek SB12D2D) with a frequency range of 100 kHz–12.4 GHz. A representative setup with the DFB QCL is shown on the top of Fig. 1. Since the lasers each accept a current modulation, and the function generator outputs a voltage modulation, a voltage-to-current transfer function H for each laser (which depends on effective impedance) required experimental determination to prevent unintentional current overloading of the light sources. The transfer function was determined by biasing the DC injection

current on the laser controller to just below the mean (I_{mean}) of the lasing threshold current I_{th} and maximum allowable current specified by the manufacturer, I_{max}, and subsequently increasing the AC (or RF) voltage amplitude by small increments until the lasing threshold was observed (no signal on the photovoltaic detector). This voltage amplitude is termed V_A. The transfer function is then calculated:

$$H = \frac{I_{mean} - I_{th}}{2V_A} \qquad (1)$$

For a scan rate of 1 MHz, the transfer function was determined to be ~11.9 mA/V for the QCL and ~2.15 mA/V for the ICL. Furthermore, we observed that the transfer function varied with modulation frequency, and this effect was pronounced with the interband cascade laser, for which H decreased by nearly a factor of five between 100 kHz and 2 MHz (shown at top of Fig. 2).

The maximum achievable peak-to-peak scan depths (in wavenumber) for the bias-tee configurations were determined for a given modulation frequency and compared to those enabled by the commercial laser drivers. The optical setup involved pitching the modulated laser radiation through a 2-in. germanium etalon and scaling the spacing of time-resolved intensity peaks by the etalon free spectral range (FSR). The peaks are then fitted to a sine function, which quantifies the modulation amplitude in the wavenumber domain [cm^{-1}]. Representative intensity signals with and
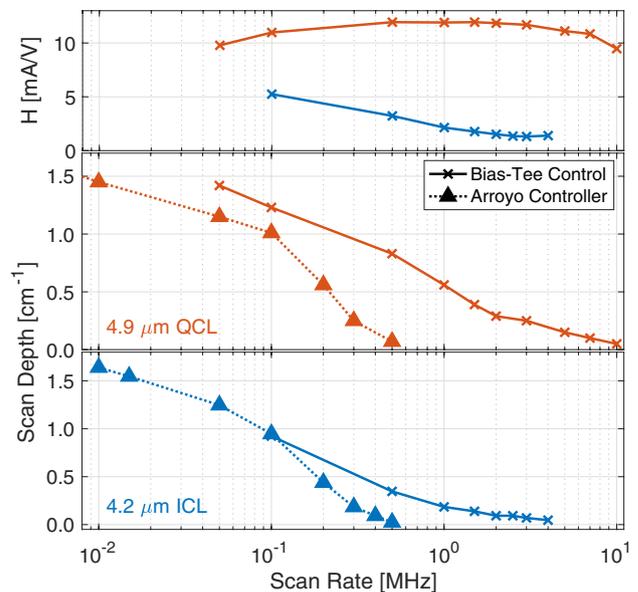
Fig. 2 Plot of voltage-to-current transfer function versus scan frequency for the bias-tee circuits (top). Plot of scan depth vs. scan frequency with and without bias-tee control for both the QCL and ICL (bottom)

without the etalon present as well corresponding wavelength modulation for the QCL are shown in the bottom of Fig. 1.

For the QCL, a modulation rate of 1 MHz produces approximately 25 peaks in the etalon signal over a time interval of approximately 300 ns over the upscan. This 300 ns represents an effective integration time for the measured spectra and inferred gas properties (at 1 MHz). To temporally resolve these etalon peaks, an optical detector with bandwidth $\geq$ 85 MHz must be utilized. In this work, detectors with bandwidth greater than 190 MHz were utilized.

The respective scan depths and transfer function of each laser were determined as a function of modulation frequency and plotted in Fig. 2. As depicted, the bias-tee configuration extends the scan frequency up to several MHz with substantial corresponding RF wavenumber modulation amplitude. Divergence in maximum achievable scan depth is observed between the two modulation schemes at frequencies above 100 kHz. For the bias-tee circuit, reference scan depths of 0.55 cm^{-1} and 0.18 cm^{-1} were achieved at 1 MHz for the QCL and ICL, respectively. During measurements in the detonation environment, the laser is scanned below its lasing threshold to account for thermal emission on the detector. We note that the phase lag between laser output intensity and wavelength (or wavenumber) renders the downscan less usable, occurring at a time of minimum laser power and yielding poor signal-to-noise ratio (SNR).

3 Spectroscopic methods

In this section, we describe the spectroscopic methods used to quantitatively infer temperature, pressure, and species density for CO and CO$_2$ from absorption data. Estimations of measurement uncertainty along with uncertainty dependencies for each of these variables (including the effects of simplifying assumptions) are presented in a detailed analysis in Appendix A.

3.1 Temperature and CO density measurement

A cluster of three P-branch transitions in the fundamental vibrational bands of CO was probed for evaluation of temperature, pressure, and CO column number density of the detonated gases. The specific rovibrational transitions are indicated in the top of Fig. 3, which shows the P(2,20), P(0,31), and P(3,14) lines where the nomenclature P(v'',J'') indicates the respective lower vibrational (v'') and rotational (J'') quanta. These CO transitions were primarily selected for their strength, relative spectral isolation from other combustion species, and divergent temperature-dependence due to their differences in lower state energy [25, 35]. Line intensities and positions are shown in Fig. 3 with representative absorbance spectra at various conditions of interest.
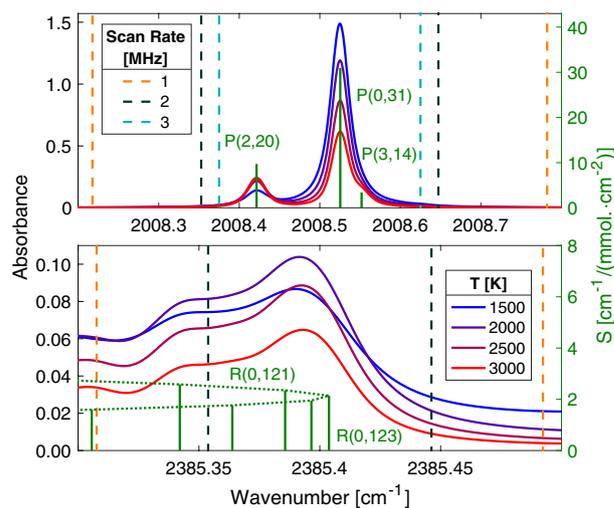
Fig. 3 Target CO and CO$_2$ absorption spectra at relevant temperatures for $X_{CO} = 0.20$, $X_{CO_2} = 0.15$, atmospheric pressure, and a 1 cm optical path-length. Linestrengths for the target transitions are plotted overlaid at 2500 K

The Beer-Lambert law, shown in Eq. 2, relates spectral absorbance α of transition i of absorbing species j to gas properties, including the number density of species j, n_j [molec $\cdot$ cm^{-3}], and temperature T [K] in a gas medium at a particular wavenumber v [cm^{-1}] [36]:

$$\alpha_{ij,v} = -\ln\left(\frac{I_t}{I_0}\right)_v = \int_0^L n_j S_{ij}(T)\varphi_{ij}(v,T,P_Y)dl \tag{2}$$

where l [cm] is the coordinate describing the position along the optical path (line-of-sight), L [cm] is the total optical path-length through the gas medium, $S_{ij}(T)$ [cm^{-1}/molec $\cdot$ cm^{-2}] is the temperature-dependent linestrength or intensity of transition i of species j, $\varphi_{ij}(v)$ [cm] is the lineshape function, and P_Y is the set of partial pressures of all species Y in the gas mixture. I_0 is the incident intensity provided by the light source, while I_t is the transmitted light intensity that exits the absorbing medium.

If the path length is known and the absorbing species is uniformly distributed along the line of sight, the terms inside the path integral in Eq. 2 may be factored out and the the absorbance can be directly related to the absorbing species number density. However, in this experiment, both the path length and the distribution of absorbing species along the line-of-sight are unknown. The gas composition can still be quantified using a quantity known as the column density, N_j [molec./cm^2] [37], which is an integral of the number density of species j along the optical line-of-sight:

$$N_j = \int_0^L n_j dl \tag{3}$$

We may also define $\bar{T}$ as the path-averaged temperature weighted by the number density of the absorbing species [37]:

$$\bar{T} = \frac{\int_0^L n_j T dl}{\int_0^L n_j dl} \qquad (4)$$

Although path-integrated, quantitative measurements of $\bar{T}$ and N_j can be directly compared to the results of computational fluid dynamics (CFD) simulations to aid in the development and refinement of multi-physical models.

Since the lineshape function, $\varphi_{ij}(\nu)$, is dependent on wavenumber, collisional partners, pressure, and temperature, it is convenient to integrate absorbance over the entire transition to yield an absorbance area A_{ij} [cm^{-1}] independent of lineshape, utilizing the fact that the spectrally integrated lineshape function is equal to 1:

$$A_{ij} = \int_{-\infty}^{\infty} \alpha_{ij,\nu} d\nu = N_j S_{ij}(\bar{T}) \qquad (5)$$

This is usually achieved in practice by fitting an assumed lineshape function to the spectra. Equation 5 is valid when the linestrength of transition i is approximately linear with temperature, such that the path-averaged number density-weighted linestrength $\overline{S_{ij}(T)}$ is approximately equal to $S_{ij}(\bar{T})$, regardless of the temperature distribution across the pathlength [37]. For the lines selected and conditions studied in this work, the linear linestrength approximation is valid to within 1% error, as discussed in Sect. A.3. For simplicity, we drop the overbar notation in all equations in this paper such that T refers to the number density weighted pathlength-averaged temperature.

If two spectral transitions (A and B) of a single species are probed, the ratio of their absorbance areas R_{AB} reduces to a function dependent only on temperature T:

$$R_{AB}(T) = \frac{A_{Aj}}{A_{Bj}} = \frac{S_{Aj}(T)}{S_{Bj}(T)} \qquad (6)$$

Temperature-dependent linestrengths $S_{Aj}(T)$ and $S_{Bj}(T)$ can be calculated from reference temperature linestrengths $S_{Aj}(T_0)$ and $S_{Bj}(T_0)$, which for all transitions used in this work are sourced from the HITEMP database [38]. Thus, by simultaneously resolving at least two transitions for species j and determining their absorbance areas, the temperature of the gas can be inferred without requiring detailed information about the broadening parameters of the lineshape, providing a measurement independent of gas composition and total pressure. With temperature inferred, a re-arranged form of Eq. 5 can be used to find species column density:

$$N_j = \frac{A_{ij}}{S_{ij}(T)} \qquad (7)$$

The accuracy and robustness of the measurements of T and N_j therefore depend on the confidence in the temperature-dependence of the transition linestrengths, $S_{ij}(T)$. The linestrengths of the P(2,20) and P(0,31) transitions and their temperature-dependent ratio R_{AB} were validated experimentally in a High-Enthalpy Shock Tube facility at UCLA over a range of temperatures up to 2300 K, as shown in Fig. 4. Details of the shock tube apparatus and operation are described in previous work [35, 39]. In both the validation experiments, as well as measurements in the target detonation environment, a scanned-wavelength direct absorption technique [40] was utilized to scan across the wavelength domain of the three transitions. Some slight nominal disagreement is noted for the values of $S_{ij}(T)$, though this was determined to be within experimental uncertainty considering the linestrength uncertainties reported in the HITEMP database [38]. Nevertheless, the measured linestrength ratio $R_{AB}(T)$ is in excellent agreement with theoretical calculations, and this line pair has been used successfully for thermometry in previous work [35].

While the measurements rely primarily on the two strongest lines, the weak P(3,14) transition becomes more significant at very high temperatures (>1800 K), contributing to the absorbance measurement $\alpha_{\nu,\text{meas}}$ and blending
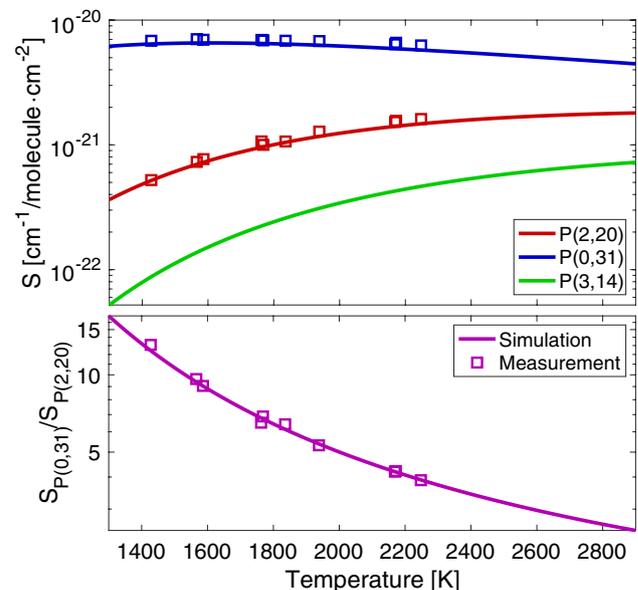
Fig. 4 Linestrengths vs. temperature for the three target transitions. The ratio of linestrengths between the P(0,31) and P(2,20) line are also shown vs. temperature. Both simulated values of the linestrength ratio using the HITEMP database [38] and measurements from the UCLA High-Enthalpy Shock Tube facility are shown
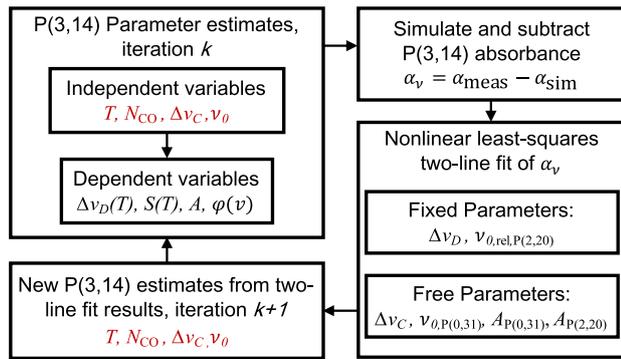
Fig. 5 Flow chart describing iterative spectral fitting procedure to account for the influence of the CO P(3,14) line in measured absorbance

with the P(0,31) line. We account for this influence with an iterative simulation procedure depicted in Fig. 5. In this procedure, the absorbance specifically associated with the CO P(3,14) transition is modeled utilizing the Voigt line-shape [41] and subtracted from the measured absorbance prior to a two-line spectral fit of the P(0,31) and P(2,20) lines. In the first step (iteration k), temperature and CO column number density, N_{CO} are estimated from Chapman-Jouguet simulations (discussed further in Sect. 3.2) and used in combination with a guess for collisional width $\Delta\nu_C$ and P(3,14) line position $\nu_{0,P(3,14)}$ to simulate the absorbance from the P(3,14) line, $\alpha_{\nu,\text{sim}}$. In the next steps, this $\alpha_{\nu,\text{sim}}$ is then subtracted from $\alpha_{\nu,\text{meas}}$, and a two-line Voigt fit is applied to the remaining P(2,20) and P(0,31) spectra to determine their respective absorbance areas A_i, which are treated as free parameters along with the P(0,31) line position $\nu_{0,P(0,31)}$ ($\nu_{0,P(2,20)}$ is fixed relative to $\nu_{0,P(0,31)}$) and a single collisional width $\Delta\nu_C$. In this study, the collision widths of all three CO lines are assumed equal; the associated consequences are discussed more in Sect. 3.2 and Appendix A.2. In the final steps, T is inferred from the ratio of fitted absorbance areas (as described by Eq. 6) and is used to obtain N_{CO} using Eq. 7, while a new estimate for $\nu_{0,P(3,14)}$ is determined from the fitted $\nu_{0,P(0,31)}$. These values of T, N_{CO}, and $\nu_{0,P(3,14)}$, along with the fitted $\Delta\nu_C$, are new parameter estimates for the next iteration (iteration $k+1$) in the loop described by Fig. 5. The iterations continue until T, N_{CO}, $\nu_{0,P(3,14)}$, and $\Delta\nu_C$ converge.

3.2 Pressure measurement

The measured collisional line-width, $\Delta\nu_C$, obtained from the aforementioned fitting procedure, contains information about the pressure of the gas medium, and is independent of the absorbance area. The collisional width is related linearly to total pressure P_{tot} as follows [36]:

$$\Delta\nu_C = P_{\text{tot}} \sum_Y X_Y (2\gamma_{\text{CO}-Y}(T)) = 2P_{\text{tot}}\gamma_{\text{CO,mix}}(T) \tag{8}$$

where $\gamma_{\text{CO}-Y}(T)$ is the temperature-dependent collisional broadening coefficient for an absorber (CO) and collision partner Y, X_Y is the mole fraction of collision partner Y, and $\gamma_{\text{CO,mix}}(T)$ is the mixture-weighted collisional broadening coefficient. Re-arranging Eq. 8, pressure can be determined given a measurement of $\Delta\nu_C$ and knowledge of the broadening coefficient for the gas mixture:

$$P_{\text{tot}} = \frac{\Delta\nu_C}{2\gamma_{\text{CO,mix}}(T)} \tag{9}$$

The temperature dependence of $\gamma_{j-Y}(T)$ in Eq. 8 for any absorbing species j is often modeled with a power-law expression [36]:

$$\gamma_{j-Y}(T) = \gamma_{j-Y,0}\left(\frac{T_0}{T}\right)^{N_Y} \tag{10}$$

where $\gamma_{j-Y,0}$ is the collisional broadening coefficient at the reference temperature T_0 (typically 296 K) and N_Y is the temperature-dependent power-law exponent (not to be confused with species column density). Both $\gamma_{j-Y,0}$ and N_Y are specific to collisional partner, as well as the quanta of the associated rovibrational transition. For CO, these parameters have been theoretically calculated by Hartmann et al. [42] as a function of rotational quantum number for high-temperatures with the collision partners CO_2, H_2O, N_2, and O_2. These tablulated values can be used with independent estimates of temperature and gas composition to determine $\gamma_{\text{CO,mix}}(T)$ in Eq. 9, and thereby determine gas pressure P_{tot}. Owing to the number of assumptions made in order to determine P_{tot} from laser absorption measurements, we provide a rigorous derivation of uncertainty estimates for all of these calculations in Appendix A.4.

Informed by the operating conditions of the methane-oxygen RDRE experiment described in Sect. 4, we estimate mixture composition of the post-detonation gases with CalTech's Shock & Detonation Toolbox [43] in CANTERA [44] using the GRI-MECH 3.0 mechanism [45]. We perform the thermodynamic calculations using a Chapman-Jouguet (CJ) detonation model assuming ambient pre-detonation conditions (300 K, 1 atm), and an initial reactant mixture composition (parameterized by the fuel-oxidizer equivalence ratio, ϕ) determined from the methane and oxygen flow rates measured in the experiment. For each operating condition, the calculation yields a post-detonation composition, temperature, and pressure. From here, we make two different assumptions to produce a range of possible mixture compositions: First, the mixture composition is frozen, while the gas is expanded isentropically to 1 atm. The frozen composition and resulting temperature comprise the

'frozen' assumption conditions. Second, the gas is allowed to equilibrate while holding entropy and pressure constant. The resulting composition and temperature comprise the 'equilibrium' assumption conditions.

For determination of $\gamma_{CO,mix}(T)$ in Eq. 9, only species with mole fractions above 0.01% in the simulation results are considered, while experimentally-measured temperature T determined from Eq. 6 is used. Considered species include CO, CO_2, H_2O, OH, H_2, O_2, O, and H. The mole fractions over ϕ from 0.6–1.6 for these species are shown as ranges in Fig. 6, reflecting variation between a frozen composition (post-detonation) assumption and an equilibrium composition assumption at one atmosphere. For broadening coefficient estimation in Eq. 9, the equilibrium mole fractions are utilized.

In reality, the detonations in the RDRE are non-ideal, as some combustion may be occurring in a deflagration mode. To assess the effect of this on the exhaust plane composition, Cantera simulations were executed for constant-pressure combustion over a range of pressures near the estimated injection pressure (3–6 atm). Again, the exhaust was isentropically expanded to one atmosphere under both a frozen and equilibrium composition assumption. In general, the ranges of mole fractions of each of the combustion species in the deflagration simulation lay within the bounds shown in Fig. 6, supporting the use of the detonation model to capture

Fig. 6 Plot of the temperature (top) and gas composition (bottom) for a CH_4/O_2 detonation gas expanded isentropically to one atmosphere. Each quantity is plotted as a range to indicate the variation in gas properties between equilibrium and frozen flow

the possible range of gas composition. Additionally, it is noted that the expansion process may not be exactly isentropic, due to effects such as heat loss and friction. However, these entropy sources (while affecting gas temperature) are not expected to significantly change gas composition.

As mentioned, calculated broadening parameters for CO with collision partners CO_2, H_2O, and O_2 are tabulated in the literature [42]. Broadening parameters for CO with the collision partner H_2 are obtained from Sur et al. [46] and are scaled to account for the higher rotational quanta in this work by multiplying by the ratio of CO-N_2 broadening for different rotational quanta from Hartmann et al. [42]. To obtain the remaining broadening parameters for CO, OH, O, and H, we scale the broadening coefficient for N_2 by the optical collision diameter, σ_{CO-Y}, between CO and species Y, and reduced mass, μ_{CO-Y} of CO and species Y through the following relationship [40]:

$$\gamma_{CO-Y}(T) = \gamma_{CO-N_2}(T)\left(\frac{\sigma_{CO-Y}}{\sigma_{CO-N_2}}\right)^2\sqrt{\frac{\mu_{CO-N_2}}{\mu_{CO-Y}}} \qquad (11)$$

The optical collision diameter σ_{CO-Y} is calculated according to intermolecular potential parameter combination rules developed for the Lennard–Jones 6-12 potential [47]:

$$\sigma_{CO-Y} = \frac{1}{2}(\sigma_{CO} + \sigma_Y) \qquad (12)$$

Although the optical collision diameter is not necessarily equal to the kinetic collision diameter, they are assumed to scale proportionally for the collision partners of interest [48]. The reduced mass is defined as

$$\mu_{CO-Y} = \frac{m_{CO}m_Y}{m_{CO} + m_Y} \qquad (13)$$

Values of σ_Y for CO, N_2, OH, O, and H are estimated from the collision diameters used in combustion species transport modeling [49], while values of m_Y are determined from species atomic and molecular weights. The uncertainties associated with this estimation procedure are included in our uncertainty analysis, discussed in more detail in Appendix A.5.

To simplify and increase the robustness of the iterative spectral fitting procedure described by Fig. 5, we assume that the collisional widths $\Delta\nu_C$ of the three target CO transitions P(0,31), P(2,20), and P(3,14) are equal to one another. This implies that the mixture-weighted collisional broadening coefficients, $\gamma_{CO-mix}(T)$, are also equal for the three rovibrational transitions. We show the validity of this assumption in Fig. 7, in which $\gamma_{CO-mix}(T)$ for each of the three CO lines is plotted as a function of temperature for an equilibrium-assumed detonation exhaust composition at a nominal operation equivalence ratio of $\phi = 1.1$. It can be seen that
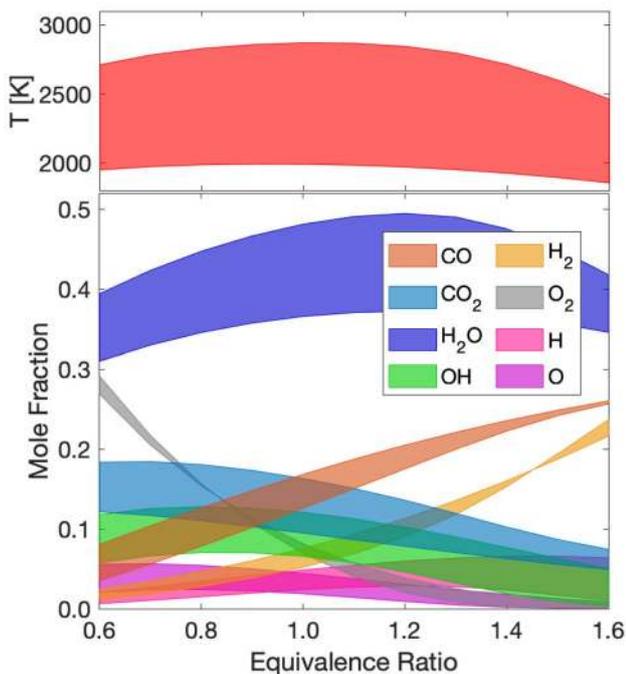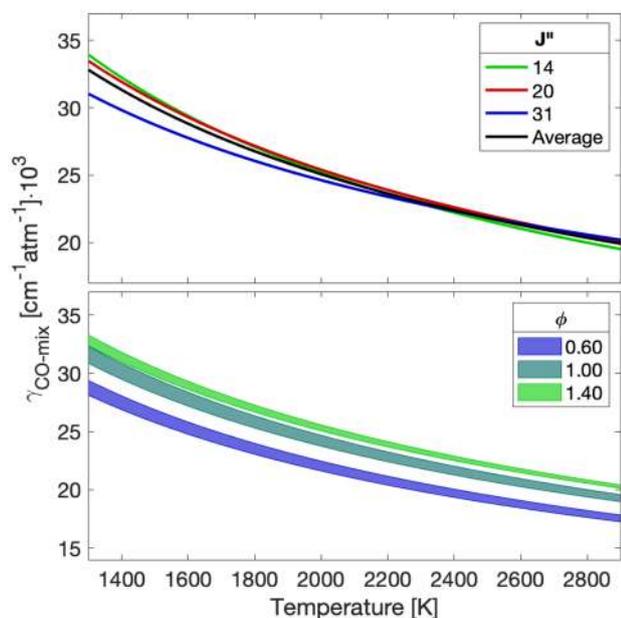
Fig. 7 $\gamma_{CO-mix}(T)$ plotted as a function of temperature for different rovibrational transitions J'' (top) as well as for different gas compositions corresponding to varying RDRE operation conditions and frozen vs. equilibrium assumptions (bottom)

the predicted values for all three lines converge within 5% at temperatures between 2000 and 3000 K, confirming the appropriateness of the assumption for the RDRE exhaust measurements performed in this work. Fig. 7 also shows the variation of γ_{CO-mix} for different equivalence ratios covering the range of frozen and equilibrium flows. It is observed that the broadening coefficient does not change significantly with species mole fraction variation associated with equivalence ratio and with frozen or equilibrium conditions, particularly at higher temperatures and equivalence ratios, reducing the error introduced with the assumption of equilibrium composition, as detailed in Appendix A.5.

3.3 CO$_2$ density measurement

A group of R-branch transitions comprising the bandhead of the $v_1 v_2^{l_2} v_3 (01^1 0 \rightarrow 01^1 1)$ fundamental vibrational band of carbon dioxide was targeted for sensing of CO$_2$ column number density in the detonated gases. The specific rovibrational transitions are indicated in the bottom of Fig. 3, which shows the R(119)-R(129) lines in the bandhead. Unlike the targeted lines for CO, the lines of CO$_2$ in this bandhead are too spectrally blended to infer temperature and mole fraction utilizing the methods outlined in Sect. 3.1. Moreover, rovibrational bandheads at high temperatures and even moderate pressures are susceptible to collision-induced rotational energy transfers that

distort molecular spectra at high collision frequencies, via a phenomenon known as line-mixing [50]. By accounting for line-mixing with additional spectral modeling, rovibrational bandheads have been successfully used to quantitatively interpret thermochemistry in rocket propulsion flows [51]. To interpret the absorption measurements of CO$_2$ in rotating detonation rocket flows, we implement a line-mixing model for the $v_1 v_2^{l_2} v_3 (00^0 0 \rightarrow 00^0 1)$ bandhead developed in prior work [52]. The model, which uses the HITEMP database [38], is a function of J''-dependent broadening parameters $\gamma_{CO_2-Y}(T)$, temperature T, total pressure P_{tot}, and number column density N_{CO_2}. The absorbance is modeled as

$$\alpha_{CO_2,\nu} = N_{CO_2} \frac{\text{Im}(\mathbf{d} \cdot \mathbf{G}^{-1} \cdot \boldsymbol{\rho} \cdot \mathbf{d})}{\pi} \tag{14}$$

where the matrix $\boldsymbol{\rho}$ and vector $\mathbf{d}$ [cm^{-1}/(molec $\cdot$ cm^{-2})]$^{\frac{1}{2}}$ are temperature dependent sets of spectral parameters that describe lower state Boltzmann population fraction and transition amplitudes. $\mathbf{G}$ [cm^{-1}] is a complex matrix defined as:

$$\mathbf{G} = \nu \mathbf{I} - \boldsymbol{\nu}_0 - i P_{tot} \mathbf{W}_{CO_2-mix}(T) \tag{15}$$

where $\mathbf{I}$ is the identity matrix, $\boldsymbol{\nu}_0$ [cm^{-1}] is a diagonal matrix of transition linecenters, and $\mathbf{W}_{CO_2-mix}(T)$ [cm^{-1}/atm] is the temperature dependent relaxation matrix, which contains mixing rates for all relevant rovibrational transitions that scale with the collisional-broadening coefficients of the transitions. Thus, with independent knowledge of the temperature, pressure, and mixture-weighted broadening parameters, the absorbance at the bandhead can be modeled as a function of a single variable (N_{CO_2}). More detail on the molecular physics governing line mixing is available in previous work [39].

Using values of $\gamma_{CO_2-Ar}(T)$ previously measured for the rovibrational transitions of interest [52] in an argon bath gas, we construct a modified relaxation matrix for the $(01^1 0 \rightarrow 01^1 1)$ bandhead based on the experimentally determined $\mathbf{W}_{CO_2-Ar}(T)$ for the neighboring $(00^0 0 \rightarrow 00^0 1)$ bandhead. The model includes measured broadening parameters from the CO$_2$ lines with rotational quanta $J'' = 99-145$, wholly encompassing the lines targeted in this work ($J'' = 117-131$). The predictive capability of this modified line-mixing model for the targeted wavelength region is examined using the high-enthalpy shock tube (described previously), and a representative case is shown in Fig. 8. The spectral simulation incorporating the line-mixing model exhibits much better agreement with the measured CO$_2$ bandhead spectra than the spectral simulation that neglects line-mixing, capturing the peak-to-valley differential absorption with lower residuals (~3%).

The relaxation matrix for Ar is scaled to determine the relaxation matrix in the RDRE exhaust mixture by
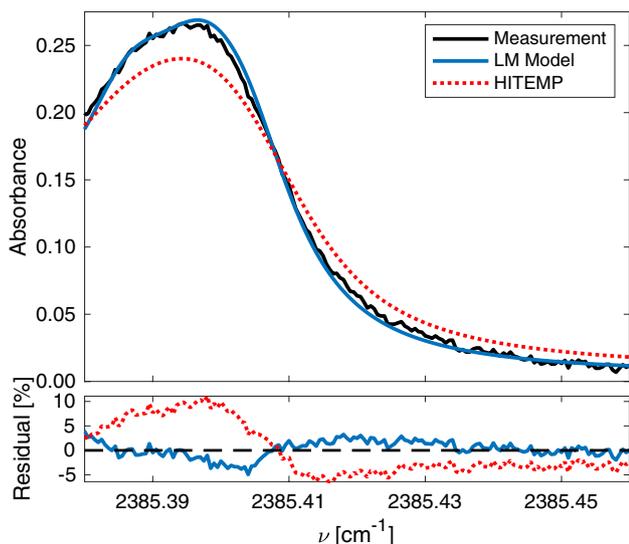
Fig. 8 Absorbance for the targeted $(01^10 \rightarrow 01^11)$ bandhead of CO_2 in an Ar bath gas measured in the UCLA High-Enthalpy Shock Tube facility, alongside predictions with and without the line-mixing model implemented. $X_{CO_2} = 0.03$, $P_{tot} = 0.95$ atm, $T = 2221$ K, $L = 10.32$ cm

$$\mathbf{W}_{CO_2-mix}(T) = \mathbf{W}_{CO_2-Ar}(T)\left(\frac{\gamma_{CO_2-mix}(T)}{\gamma_{CO_2-Ar}(T)}\right) \quad (16)$$

Here, $\gamma_{CO_2-Ar}(T)$ is the collisional broadening coefficient for CO_2 in Ar and $\gamma_{CO_2-mix}(T)$ is the mixture-weighted collisional broadening coefficient for CO_2, defined as

$$\gamma_{CO_2,mix}(T) = \sum_Y X_Y(\gamma_{CO_2-Y}(T)) \quad (17)$$

$\gamma_{CO_2-Y}(T)$ for the collision partners CO_2, H_2O, N_2, and O_2 are obtained using tabulated values for $J'' = 101$ provided by Rosenmann et al. [53] and $\gamma_{CO_2-Ar}(T)$ is obtained using measured values for collisions with argon at $J'' = 101$ [52]. Broadening parameters for CO_2 with collision partner H_2 are determined using the same method as those for CO—the $\gamma_{CO_2-H_2}(T)$ value reported by Sur et al. [46] is scaled to account for the higher rotational quanta in this work. As with CO, the remaining CO_2 broadening parameters for collision partners CO, OH, O, and H are estimated by scaling $\gamma_{CO_2-N_2}(T)$ according to Eq. 11 through 13. The mole fractions X_Y are estimated from the CJ detonation model described in Sect. 3.2.

For every wavelength modulation period, the measured temperature and pressure from the previously discussed CO spectroscopy, as well as estimated mixture composition (determined through the methods described in Sects. 3.1 and 3.2) are used as inputs for the line-mixing model for CO_2. The line-mixing model is fitted to the measured spectra using a nonlinear least-squares solver with N_{CO_2} as a free
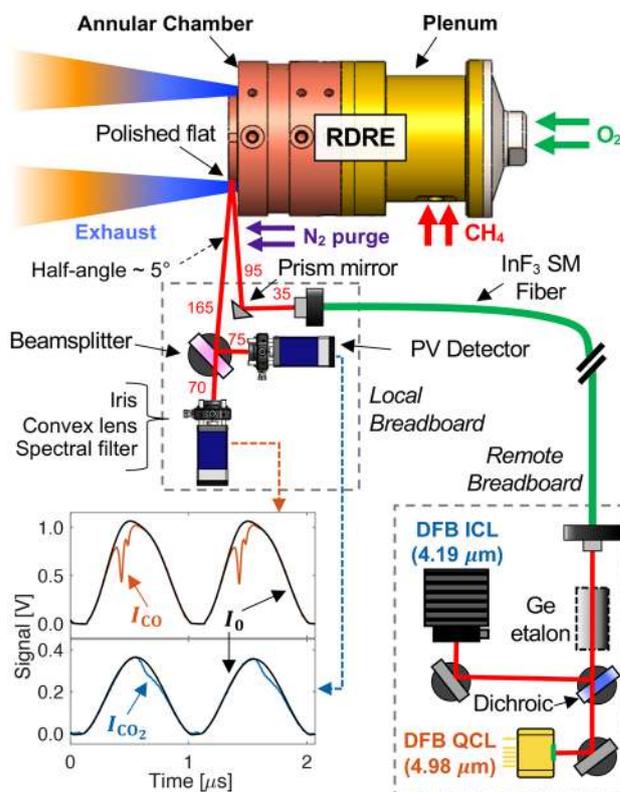
Fig. 9 Optical interface for RDRE data collection. Beam path lengths are provided in millimeters

parameter, while holding T and P_{tot} constant. To simplify the fitting procedure, a peak-to-valley differential absorption is specifically targeted, wherein only the absorbance at the bandhead peak (≈ 2385.39 cm^{-1}) and at a low-absorbance valley region (≈ 2385.50 cm^{-1}) are used for the fit. Due to the larger number of assumptions and estimates for the inputs to the CO_2 spectral model, the inferred column density has inherently higher uncertainty, as discussed in Appendix A.6.

4 Experimental setup

Figure 9 illustrates the optical configuration for the absorption sensing technique and hardware interface for conducting measurements at the exit plane of an RDRE combustor. The design of the modular RDRE test article is described thoroughly in previous work [7, 12], and so only the information most relevant to the optical interface, operating conditions, and data analysis are detailed here for brevity. The outer diameter of the copper test article annulus is 7.62 cm, and the width of the annulus is 0.5 cm. The RDRE operates on gaseous methane (CH$_4$) and gaseous oxygen (O$_2$) as the main propellants, which are ignited with a pre-detonation

system near the exit of the chamber. The propellants are injected through impingement-style elements around the annulus, and their flowrates are measured using sonic orifices. These measured flow rates are used to determine overall operating equivalence ratio, ϕ. During a test, pressures in the injection manifolds are high enough to provide choked flow, though this may not be the case during the presence of a passing detonation wave. Capillary tube attenuated pressure (CTAP) static probes are used to monitor pressure at various locations in the annular combustion chamber. Additionally, measurements of the test article thrust are made using a 500 lbf load cell.

A notable feature of the RDRE hardware is the polished copper center body protruding out of the exit plane. Four $0.635\,\text{cm} \times 0.635\,\text{cm}$ square flats are machined onto the centerbody, providing retro-reflective surfaces for the laser beams. As the annular gap is 0.5 cm, the optical path length is approximately 1 cm.

To probe the targeted lines of CO near 4.98 μm and the CO_2 bandhead near 4.19 μm, the DFB QCL with ~50 mW output power and the DFB ICL with ~5 mW output power described in Sect. 2 are utilized as the single-mode light sources, respectively. A dichroic filter is used to multiplex the laser beams, acting as a beamsplitter with minimal power loss. Both incident beams are aligned colinearly and free-space coupled into one single-mode InF$_3$ fiber with a 9 μm core diameter. The fiber delivers the light from a remote breadboard, on which the lasers are mounted, to a local breadboard mounted to the RDRE thrust structure. The fiber output is then re-collimated using a CaF$_2$ lens and reflected off a small right-angle prism mirror. The beam is then pitched across the exit of the RDRE annulus through the exhaust gases and onto the polished center body flat surface, which reflects the light back towards the detector assembly, as shown in the top of Fig. 9. A beam splitter separates the transmitted light so that each beam can be spectrally filtered for its respective wavelength (Electro Optical Components, 4210 ± 42 nm and Spectrogon, 4960 ± 148 nm) before being collected on distinct thermo-electrically cooled photodetectors. The spectral filters also mitigate interference caused by thermal emission from the hot exhaust gases. The two MCT photovoltaic detectors (Vigo PVMI-4TE-8-1x1) have ~200 MHz bandwidth each to resolve the RF modulation. The pitch and catch optics (detectors, beamsplitter, prism mirror, lenses) were all mounted on the aforementioned local breadboard using standard optical posts adjusted in height to be in a horizontal plane passing through the centroid of the RDRE. The optical setup includes kinematic mounts for beam pointing and translation, which were used to optimize alignment and maximize the transmitted light intensity during the experiment.

Raw detector voltages were collected at sample rates of 250 MS/s and 500 MS/s, for 1.0 s intervals (0.5 s intervals for 500 MS/s tests) of hot-fires spanning approximately 1.0 s in duration. A nitrogen purge system directed along the side of the test article displaces ambient H_2O vapor and CO_2 and mitigates exhaust gas recirculation in the optical line-of-sight, which can otherwise spectrally interfere with the absorbance spectra of CO and CO_2, respectively. The QCL targeting CO is modulated at rates varying from 1 to 3 MHz, while the ICL targeting CO_2 is modulated at 1 MHz. Prior to each test, the incident light intensity I_0 is recorded for each light source, along with a measurement of the light intensity with the germanium etalon in the line-of-sight to determine the relative frequency of the laser scan.

5 Results and discussion

Time-resolved laser absorption measurements were performed on the RDRE combustor over a range of propellant flow rates ($\dot{m} = 0.2-1.0$ lbm/s) and mixture ratios ($\phi = 0.6-1.6$) with CH$_4$/GOx as propellants. All tests were completed at the Air Force Research Laboratory on Edwards Air Force Base in Edwards, CA USA. Raw detector voltage data, such as those shown in the inset of Fig. 9, are processed using Eq. 2 to obtain spectral absorbance α_ν for both species of interest. We note that the transmitted light intensity I_t required subtraction of thermal emission and the background light intensity I_0 required temporal shifting and multiplication by a scalar to match the non-absorbing portion of the transmitted intensity. Due to the large frequency separation between laser modulation and environmental noise, common baseline convoluting factors such beam steering appear frozen during a single modulation period and do not distort the scan shape (enabling correction by a simple scalar multiplier).

In this section, we first present time-histories of temperature, CO, and pressure calculated from the absorption measurements provided by the QCL at MHz rates, stepping through the intermediate analyses required to determine those values. We then follow with a demonstration of simultaneous multi-species CO and CO_2 sensing enabled by the additional absorption measurements provided by the ICL and revealing ability to account for total carbon oxidation. Finally, we demonstrate enhanced time resolution of the technique, pushing the thermochemistry measurements to rates up to 3 MHz. As mentioned previously, a rigorous uncertainty analysis for the reported values of temperature, column number density, and pressure is presented in Appendix A.

5.1 Time-resolved CO spectroscopy

The spectra targeting CO are fitted according to the iterative procedure described in Sect. 3.1 and by Fig. 5. Figure 10
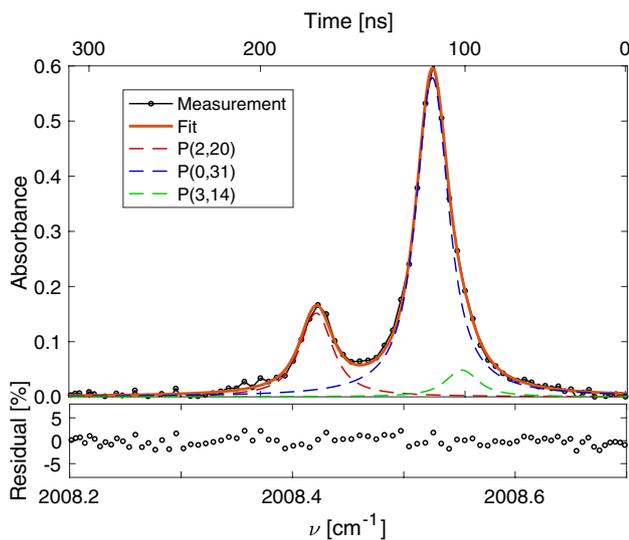
Fig. 10 Example scanned-wavelength Voigt fitting of data from the RDRE experiments, showing an effective measurement integration time of 300 ns
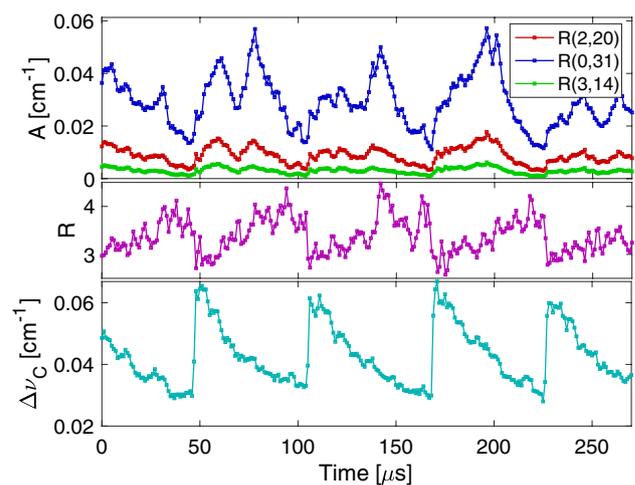
shows the measured absorbance spectra from a representative single sub-microsecond scan (no averaging) along with the corresponding spectral fits of the three targeted CO transitions. The residual between measurement and overall spectral fit with the Voigt lineshape model is typically under 2%, demonstrating the appropriateness of the iterative fitting procedure for this sensing application and the relatively high SNR. The behavior of the CO spectra as the detonation waves pass through the line-of-sight can be visualized more readily by plotting the spectra in three dimensions as a function of time, as shown in Fig. 11. A distinct periodicity
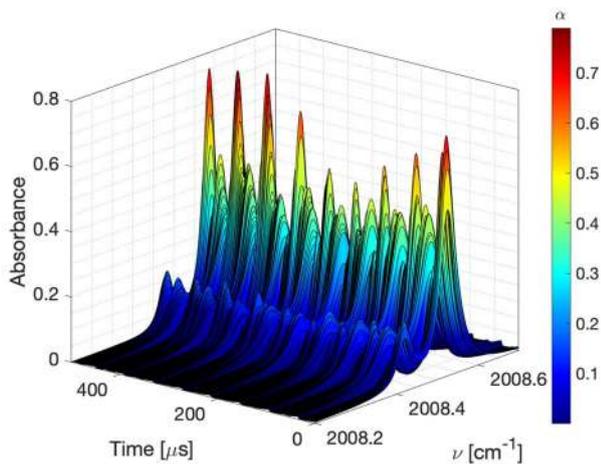
in the time-resolved behavior of the spectra is observed, evidenced by sharp increases in both the peak absorbance α and the collisional broadening in the lines. The rapidly changing thermodynamic conditions in the flowfield associated with each detonation cycle affect the spectral parameters for each transition differently, which can be discerned by plotting absorbance area A_{ij} and collisional width $\Delta\nu_C$ as a function of time for the P(0,31), P(2,20) and P(3,14) lines, as shown in Fig. 12. As with the spectral absorbance shown in Fig. 11, periodic behavior is observed in time for all absorbance areas A_{ij}, with the the P(0,31) and P(2,20) lines consistently demonstrating the largest values in every detonation cycle. The fitted collisional width $\Delta\nu_C$ for all lines shows a very clear sharp rise and decay behavior, indicative of a large pressure rise associated with a shock or detonation wave. The ratio of the absorbance areas for the P(0,31) and P(2,20) lines, R, is also plotted as a function of time in Fig. 12. At the start of every cycle, there is a distinct drop in R associated with an increase in temperature, as indicated by temperature-dependence shown in Fig. 4.

Once temperature is determined from R, column number density N_{CO} and total pressure P_{tot} can be determined via the methods described in Sects. 3.1 and 3.2, respectively. Representative results are shown in Fig. 13 for 1000 μs of a hot-fire test conducted with a propellant mass flow rate of $\dot{m} = 0.6$ lbm/s and a nominal operating equivalence ratio of $\phi = 1.1$. For this test, periodicity in temperature, column density, and pressure characteristic of the cyclic nature of RDREs are readily observed. Precision error for all variables is calculated by dividing measurement noise (1-σ of a 5-point moving average) by the mean variable value for the entire test. Measured temperature
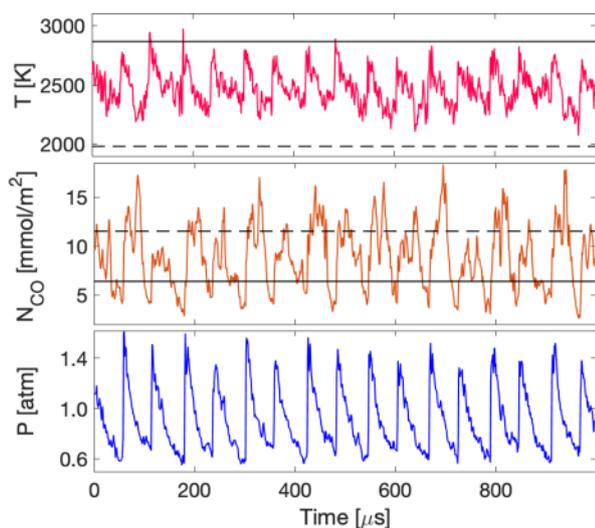

Fig. 11 Visualization depicting changing spectra of the P(0,31), P(2,20) and P(3,14) lines of CO in time during a representative measurement of RDRE exhaust


Fig. 12 Time-resolved absorbance areas of the P(0,31), P(2,20) and P(3,14) lines of CO (top). The time-resolved ratio of absorbance areas of the P(0,31) and P(2,20) lines (middle). Time-resolved collisional-width (bottom)

Fig. 13 Time-resolved temperature (top), CO column density (middle) and pressure over 1000 μs. The temperature and column density values predicted from CANTERA at $P_{tot} = 1$ atm are shown for equilibrium flow as solid black curves and for frozen flow as dashed black curves. A path length of 1 cm is assumed for the column density

is observed to oscillate between 2250 and 2800 K with a precision error of approximately 2.1%, and nominally within the bounds set by the frozen and equilibrium conditions predicted by the CJ detonation model. Likewise, the CO column number density oscillates about the range of predicted values with a precision error of about 3.1%. Additionally, there is a noticeable second peak in N_{CO} in many of the cycles. The time-history of the total pressure determined from fitted collisional width $\Delta\nu_C$ shows very sharp peaks to values as high as 1.5 atm and decay to valleys as low as 0.6 atm, with a precision error of approximately 3.7%. Uncertainty associated with these measurements is detailed in Appendix A.

A harmonic analysis of the thermodynamic conditions can allow us to examine these distinct behaviors among the thermodynamic state variables in more detail. A discrete-Fourier transform is performed on a 10 ms interval of the temperature, column number density, and pressure time-histories, and the resulting dominant temporal frequencies [kHz] are shown in Fig. 14. For this RDRE test, the single-sided amplitude spectra of these thermodynamic state variables reveals common peaks at 16.78 kHz as well as associated overtone frequencies (33.56 kHz, 50.34 kHz, 67.12 kHz, etc.). Interestingly, although 16.78 kHz represents the strongest frequency for both temperature and pressure and corresponds to the detonation frequency determined through high-speed video [12], the strongest frequency observed for CO column number density is 33.56 kHz, likely a consequence of the second peak observed in N_{CO} during many of the detonation cycles, as shown in Fig. 13.
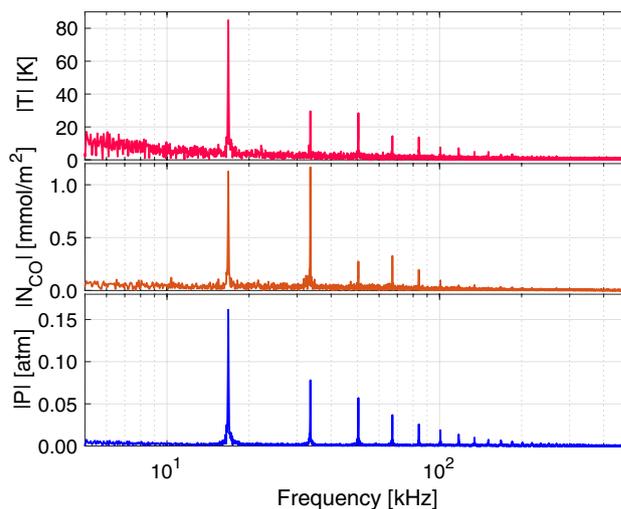
Fig. 14 Fast-Fourier transform of 10 ms of time-resolved temperature, CO column density and pressure data. A strong peak near 16.78 kHz is observed

5.2 Simultaneous CO and CO$_2$ measurement

To achieve simultaneous measurement of CO$_2$, the spectra targeting CO$_2$ are fitted with a line-mixing model using the time-resolved thermodynamic parameters measured from the CO spectra as inputs, as described in Sect. 3.3. Fig. 15 shows the measured absorbance spectra from a representative single scan along with the least-squares fit of the line-mixing model. A corresponding simulation of the spectra
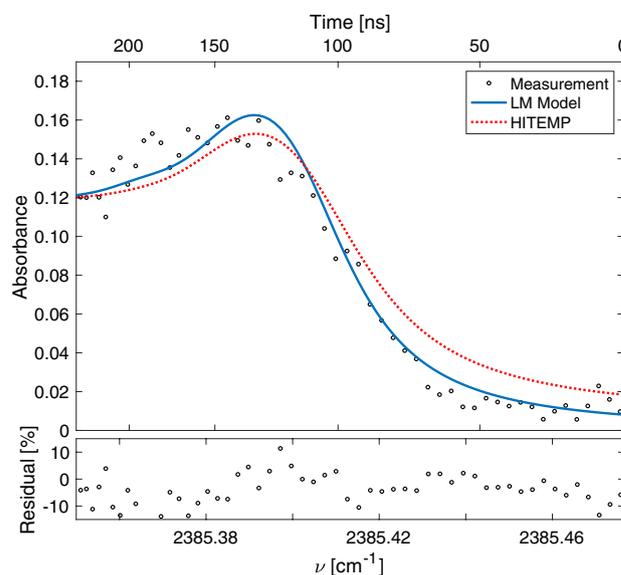

Fig. 15 Example scanned-wavelength CO$_2$ bandhead data from the RDRE experiments, showing an effective measurement integration time of 250 ns

without implementing the line-mixing model is also shown, highlighting the line mixing model's ability to better capture differential absorption between the maximum and minimum absorbance regions in the CO_2 bandhead spectra. The signal-to-noise ratio (SNR) of the measurement is much lower than that of CO, resulting in spectral fit residuals of approximately 10%. There are a few causes, including the low detector signal of the laser light intensity from the ICL as shown in Fig. 9 and the generally lower CO_2 absorbance relative to that of CO for these thermodynamic conditions. Nevertheless, the absorbance measurement can be quantitatively interpreted to provide a time-resolved measurement of CO_2 density in the detonation exhaust with a measurement precision of approximately 6.2%. To better quantitatively interpret the relative concentrations of CO and CO_2 and separate the time-resolved species concentration behavior from the time-resolved temperature and pressure, we normalize the CO and CO_2 column densities by the ratio of pressure and temperature to yield $\widetilde{N}_j$:

$$\widetilde{N}_j = N_j \frac{k_B T}{P_{\text{tot}}} \tag{18}$$

which we expect to trend with the relative concentration or mole fraction of species across the line-of-sight.

Representative $\widetilde{N}_{\text{CO}}$ and $\widetilde{N}_{\text{CO}_2}$ values from a hot-fire test conducted with a propellant mass flow rate of $\dot{m} = 1.0$ lbm/s and an equivalence ratio of $\phi = 1.1$ are shown in Fig. 16 along with their sum. Important trends among the simultaneous species measurements are immediately noted; periodic spikes in CO correspond to dips in CO_2, while their sum (total) oscillates with a lower amplitude about a constant value, indicating a conservation of total carbon oxides in the RDRE exhaust with some potential variation
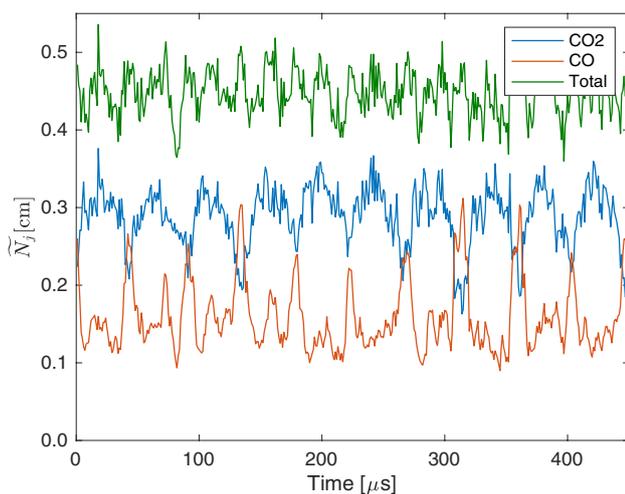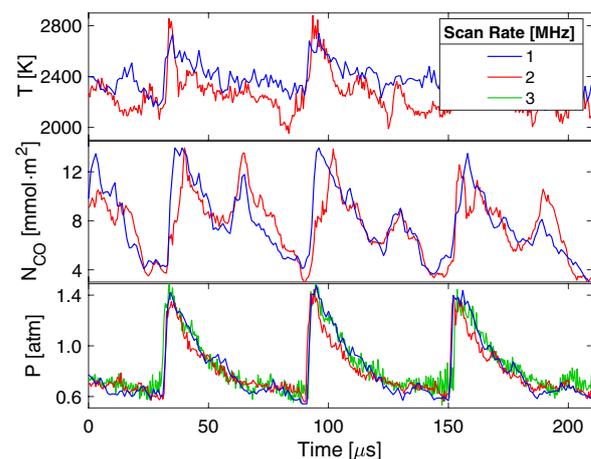
in oxidizer-to-fuel ratio over time. The power of the simultaneous CO/CO_2 sensing strategy coupled with the MHz-measurement rates is highlighted by examining intra-cycle species evolution. In each cycle, a sudden large increase in CO is immediately followed by an increase in CO_2 which occurs on a longer timescale as CO decreases. As was seen in Figs. 13 and 14, some cycles exhibit a second—albeit less pronounced—increase and decrease in CO accompanying the larger increase and decrease, implying some potential chemical kinetic evolution within each cycle (convolved with post-detonation fluid dynamics). It should further be noted that chemistry (carbon oxidation) in the exhaust plume (related to entrained air) may influence the ratio of CO and CO_2 and their quantitative comparison. Such a biasing effect is minimized by the nitrogen purge and close axial proximity of the beam to the RDRE chamber.

5.3 Multi-MHz sensing

To demonstrate the high-speed RF wavelength modulation capability of the opto-electronic configuration used in this work, we conducted scanned-wavelength direct absorption spectroscopy measurements of the target CO lines at 1, 2, and 3 MHz using the DFB QCL. Fig. 17 shows the measured temperature, CO column number density, and pressure time-history of three independent RDRE tests operating at the same mass flow rate of $\dot{m} = 0.6$ lbm/s and reactant equivalence ratio of $\phi = 1.1$. The time-histories in Fig. 17 have been phase-adjusted for simpler comparison amongst the measurements. In addition, the values of P_{tot} have been plotted as deviation about their common mean. As noted in Fig. 2, the scan depth of the QCL decreases as the scan rate increases—for the 3 MHz measurements, the P(0,31) and P(3,14) lines were only partially resolved. This reduced the

Fig. 16 Time-resolved profiles of temperature and pressure normalized column number densities $\widetilde{N}_j$ for CO, CO_2, and their sum

Fig. 17 Time-resolved temperature, CO column density, and pressure at the RDRE exhaust for 1, 2, and 3 MHz measurement rates. Pressure is shown as a deviation from mean pressure

robustness of the spectral fit and introduced more noise into the time-histories of absorbance area A_{ij} and thereby more noise into the area ratio R, precluding clean measurements of T and N_{CO}. Fortunately, the spectral fits of collisional width $\Delta\nu_C$ were found to be more robust against this phenomenon, since the P(2,20) line was completely resolved, enabling 3 MHz measurement rates of total pressure P_{tot} using the single line (with a modest increase in uncertainty). Some test-to-test and cycle-to-cycle variation is observed between the three experiments; however, distinct common thermochemical behavior is observed, most notably the secondary peak in the N_{CO} time-histories. The higher speed measurements clearly show a resolution of sharp changes in temperature and species density, as well as the peaks and valleys of the pressure rise and fall associated with each of the detonation waves (capturing temporal behavior more difficult to resolve at the lower measurement rates).

6 Summary

A laser absorption sensing strategy for CO, CO_2, temperature, and pressure has been developed for MHz measurements in annular detonation exhaust flows using diplexed RF modulation (bias-tee circuitry) with mid-infrared distributed feedback lasers. Temperature, pressure, and CO column number density were inferred from an iterative multi-line Voigt fitting procedure applied to a spectrally-resolved cluster of P-branch transitions in the fundamental infrared band near 4.98 μm. CO_2 column number density measurements were obtained by fitting a line-mixing model of absorption to the peak and valley of the rovibrational bandhead near 4.19 μm, using the temperature and pressure inferred from CO as inputs. The multi-parameter sensing method was demonstrated on a rotating detonation rocket combustor at measurement rates up to 3 MHz with integration times as short as 100 ns, elucidating transient gas properties not previously observable. Beyond the unique application, the RF modulation technique using bias-tee circuitry with mid-infrared DFB sources was proven both exceptionally fast and robust, with broader utility to other highly transient harsh environments.

Appendix: Uncertainty analysis

In this paper, we present measurements of temperature, pressure, and species column number density in rotating detonation rocket flows. To facilitate comparison with modeling and simulation, we provide experimental uncertainties for each of these measurements, and detail how they are calculated in this Appendix. The uncertainty analysis presented here largely follows that of Pineda et al. [35]; however, here we provide more rigorous treatment of uncertainty in spectral fitting parameters, added discussion for accounting for blended spectra, and new information regarding estimating pressure from measured collisional width. As in that work, unless otherwise noted, we follow the Taylor series method (TSM) of uncertainty propagation [54], in which the uncertainty of a variable r, Δr, is given by:

$$(\Delta r)^2 = \left(\frac{\partial r}{\partial x_1}\Delta x_1\right)^2 + \left(\frac{\partial r}{\partial x_2}\Delta x_2\right)^2 + \cdots \quad (19)$$

where x_i are independent variables and Δx_i are their respective uncertainties. A visual summary of the relative experimental uncertainties for each variable is shown in Fig. 18, in which the individual contributions from dependent variables are highlighted and discussed in greater detail in the following subsections.

Linestrength uncertainty

For each species j, uncertainty in temperature-dependent linestrengths, $\Delta S_i(T)$, for each line i can be calculated from the expression for temperature-dependent linestrength:

$$S_i(T) = S_i(T_0)\frac{Q(T_0)}{Q(T)}\exp\left[-\frac{hcE_i''}{k_B}\left(\frac{1}{T} - \frac{1}{T_0}\right)\right]$$
$$\times \left[1 - \exp\left(\frac{-hc\nu_{0,i}}{k_BT}\right)\right] \quad (20)$$
$$\left[1 - \exp\left(\frac{-hc\nu_{0,i}}{k_BT_0}\right)\right]^{-1}$$

where Q is the partition function for the molecule of interest, and $\nu_{0,i}$ is the linecenter of the transition i of interest.

The two uncertainties with which we are primarily concerned are the reference temperature linestrength uncertainty $\Delta S_i(T_0)$ (available in the HITEMP database [38] for the lines used in this work) and the uncertainty in
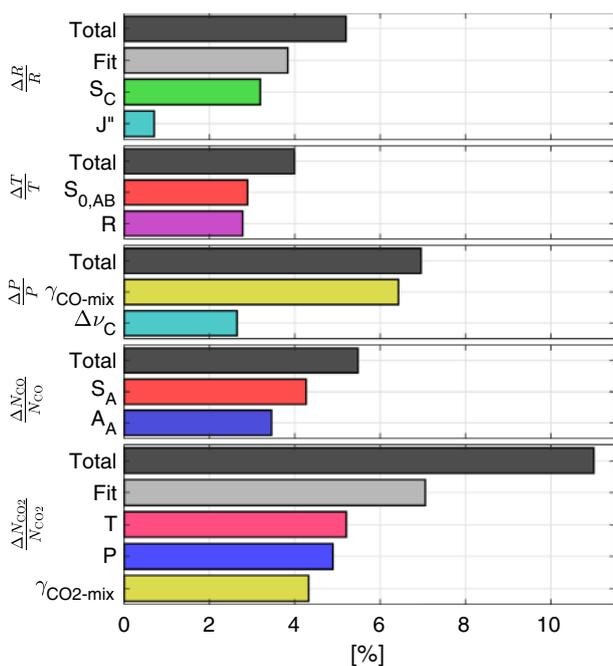
Fig. 18 Representative uncertainties for linestrength ratio R, temperature T, column density N_{CO}, total pressure P_{tot}, and column density N_{CO_2} performed on the test shown in Fig. 16. Note: these values are averaged over a time series of measurements

temperature-dependent linestrength due to uncertainty in temperature ΔT (from the uncertainty in ΔR, discussed in Sect. A.2). We assume uncertainties in lower state energies E_i'' and line positions ν_0 are secondary and negligible contributors. The total uncertainty in the linestrength $S_i(T)$ can the be calculated by summing both primary uncertainties in quadrature:

$$\left(\frac{\Delta S_i(T)}{S_i(T)}\right)^2 = \left(\frac{\Delta S_i(T_0)}{S_i(T_0)}\right)^2 + \left(\frac{\partial S(T)}{\partial T}\frac{\Delta T}{S_i(T)}\right)^2 \quad (21)$$

For CO, the linestrengths of the P(0,31), P(2,20), and P(3,14) lines are known to within 2%, 5%, and 10%, respectively, and so $\Delta S_i(T_0)/S_i(T_0) = 0.02$ for the P(0,31) line, 0.05 for the P(2,20) line, and 0.10 for the P(3,14) line.

Temperature uncertainty

In this work, temperature is determined numerically from Eqs. 6 and 20 by simulating linestrength $S_i(T)$ for the lines of interest using the HITEMP database [38] and comparing to the measured absorbance area ratio R. It can be seen that $R(T)$ is nonlinear, and the absolute value of dR/dT decreases as T increases. Practically speaking, this increases the sensitivity of T to R, such that a given absolute deviation in R, ΔR, will produce larger deviations in T, ΔT, at higher T. To more rigorously quantify the measurement uncertainty in

temperature associated with this and other factors, we can examine an analytical expression for temperature, given by [36]:

$$T = \frac{\frac{hc}{k_B}(E_B'' - E_A'')}{\frac{hc}{k_B}\frac{(E_B'' - E_A'')}{T_0} + \ln(R) + \ln\left(\frac{S_B(T_0)}{S_A(T_0)}\right)} \quad (22)$$

This expression neglects stimulated emission and is used only for sensitivity analysis. In this Appendix, we use the subscripts A, B, and C to refer to line-specific parameters for the CO P(0,31), P(2,20), and P(3,14) lines, respectively. Uncertainty in measured temperature as expressed in Eq. 22 is assumed to be dominated by the uncertainties of the reference temperature linestrengths in the HITEMP database, $\Delta S_i(T_0)$, and the uncertainty in the ratio of calculated absorbance areas ΔR:

$$\left(\frac{\Delta T}{T}\right)^2 = \frac{\left(\frac{\Delta R}{R}\right)^2 + \left(\frac{\Delta S_A(T_0)}{S_A(T_0)}\right)^2 + \left(\frac{\Delta S_B(T_0)}{S_B(T_0)}\right)^2}{\left(\frac{hc}{k_B}\frac{E_B'' - E_A''}{T_0} + \ln(R) + \ln\left(\frac{S_B(T_0)}{S_A(T_0)}\right)\right)^2} \quad (23)$$

Uncertainties in lower state energies E_i'' and physical constants are not considered. Eq. 23 implies that ΔT decreases with increasing difference in lower state energy $E_B'' - E_A''$ and increasing linestrength ratio R, highlighting the importance of line selection for accurate temperature measurements. ΔR is given by the expression:

$$\left(\frac{\Delta R}{R}\right)^2 = \left(\frac{\Delta A_A}{A_A}\right)^2 + \left(\frac{\Delta A_B}{A_B}\right)^2 \quad (24)$$

Thus, we are primarily concerned with the determination of ΔA_i, which for time-resolved scanned direct-absorption spectroscopy can be determined as $\Delta A_{i,fit}$, equal to the 1-σ standard deviation of the nonlinear least-squares parameter estimate for A_i from the Voigt fitting procedure. However, for the measurements reported here, there is additional uncertainty associated with the subtraction of the absorbance due to the P(3,14) line that appears appreciably at temperatures above ~1800 K and from the assumption that the collision widths of all three lines are equal. The overall uncertainty in absorbance area is expressed as:

$$(\Delta A_i)^2 = (\Delta A_{i,fit})^2 + (\Delta A_{i,C})^2 + (\Delta A_{i,J''})^2 \quad (25)$$

where $\Delta A_{i,C}$ is the variation in A_i resulting from the uncertainty in the simulated absorbance from the P(3,14) line and $\Delta A_{i,J''}$ is the variation in A_i resulting from the variability in the collision widths between lines.

In practice, $\Delta A_{i,C}$ is found by re-fitting the spectra after varying the linestrength of the P(3,14) line by ±10% and finding the corresponding change in A_i. Likewise $\Delta A_{i,J''}$ is found by constraining one $\Delta \nu_{C,i}$ to be higher or lower than the others

in the fitting routine by a percentage corresponding to the temperature-dependent variance in collision width across the three spectral transitions, as indicated in Fig. 7. The resulting area variations are added in quadrature to obtain $\Delta A_{i,J''}$.

For the experimental data presented in this work, it can be seen in Fig. 18 that the largest influence on the magnitude of ΔR is associated with the spectral fit, while the next largest influence is the uncertainty of the linestrength of the P(3,14) line in the HITEMP database [38]. A scatterplot of $\Delta T/T$ versus T is shown in Fig. 19, showing a range of uncertainty that tends to slightly increase with absolute temperature, and having a mean magnitude of approximately 4%.

Uncertainty in path-integrated measurement

As mentioned in Sect. 3.1, the temperature measured in this work is a CO number density-weighted path-averaged temperature. In deriving Eq. 5 from Eq. 2, we made the following implicit assumption:

$$S_{ij}(\overline{T}) \approx \overline{S_{ij}(T)} = \frac{\int_0^L n_j S_{ij}(T)dl}{\int_0^L n_j dl} \quad (26)$$

which states that the number density-weighted path-averaged linestrength is equal to the linestrength evaluated at the number density weighted path-averaged temperature. This assumption will hold regardless of the temperature distribution along the line-of-sight if the linestrength is linear in temperature across the temperature distribution [37]. To validate this, linear temperature distributions were generated spanning 500 K for various average temperatures across a hypothetical 1 cm line-of-sight. Number density was allowed to vary with temperature. $\overline{T}$ and $\overline{S_{ij}(T)}$ (for the P(0,31), P(2,20) and P(3,14) lines) were computed numerically using

Eqs. 4 and 26. $S_{ij}(\overline{T})$ was computed using Eq. 20 for the various lines. The relative difference between $\overline{S_{ij}(T)}$ and $S_{ij}(\overline{T})$ was then calculated for each average temperature. This is plotted in the top of Fig. 20. Disagreements are below 1% for mean temperatures ranging from 2000 to 3000 K.

Similarly, the temperature corresponding to each absorber density-weighted path-integrated linestrength (for the P(0,31) and P(2,20) lines) was calculated by inverting Eq. 20. Additionally, the temperature corresponding to the ratio of the absorber density-weighted path-integrated linestrengths (which is the same as the ratio of measured absorbance areas R) was calculated. The difference between these temperatures and the actual absorber density-weighted path-averaged temperature of the distribution were calculated and
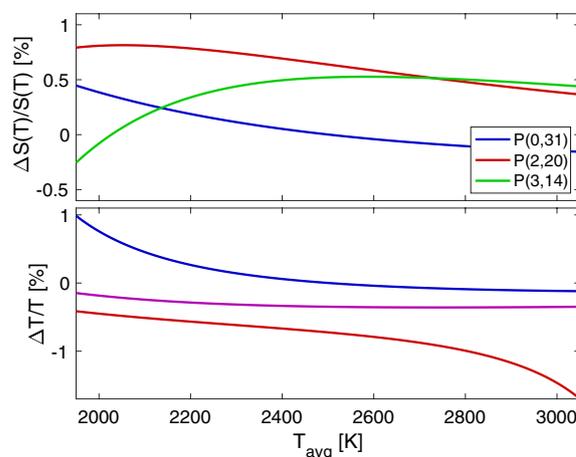
Fig. 20 The relative difference between $\overline{S(T)}$ and $S(\overline{T})$ for the P(0,31), P(2,20) and P(0,31) (top) and the difference between $\overline{T}$ and the temperature inferred from the $\overline{S}$ for the P(0,31) line (blue), the P(2,20) line (red) and from their ratio (purple)
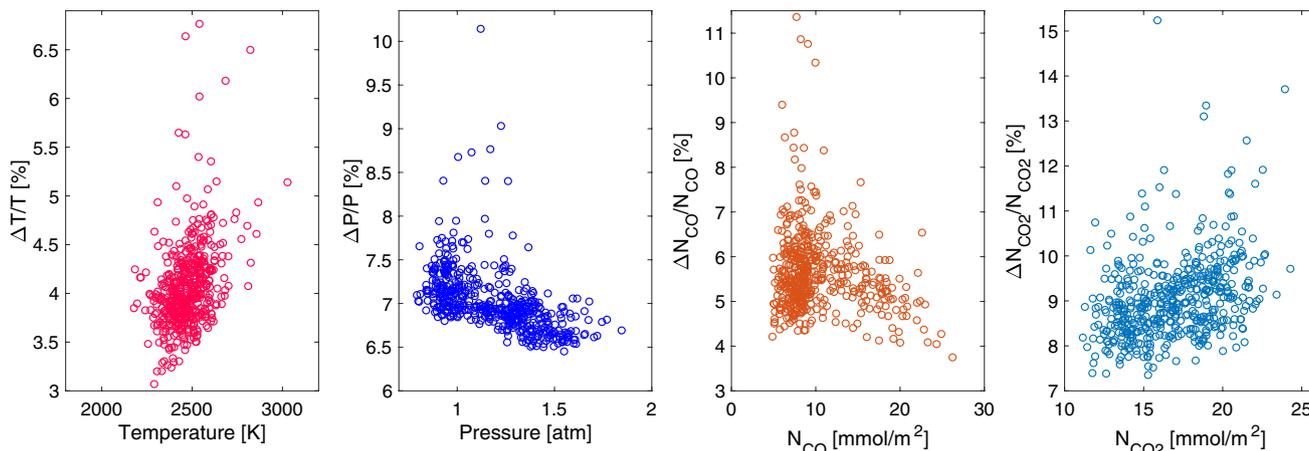
Fig. 19 Relative experimental uncertainty distributions for temperature, CO and CO_2 column number density and pressure for the test shown in Fig. 16

plotted on the bottom of Fig. 20. While the errors associated with each individual lines ranged from 0.1–1.5%, the error between the temperature inferred from the absorbance area ratio and the actual path-averaged temperature was below 0.4% for all average temperatures between 2000 and 3000 K. Due to the low values of this error relative to other experimental errors calculated in Sect. A.2, it was omitted from the remainder of the uncertainty analysis. This low disagreement validates that the measurement strategy is capable of accurately retrieving $\overline{T}$, which may be compared with 3D flowfield simulations.

Pressure uncertainty

The uncertainty in P_{tot} calculated by Eq. 9 depends on the uncertainties of $\Delta\nu_C$ and $\gamma_{\text{CO}-\text{mix}}(T)$:

$$\left(\frac{\Delta P_{\text{tot}}}{P_{\text{tot}}}\right)^2 = \left(\frac{\Delta(\Delta\nu_C)}{\Delta\nu_C}\right)^2 + \left(\frac{\Delta\gamma_{\text{CO}-\text{mix}}(T)}{\gamma_{\text{CO}-\text{mix}}(T)}\right)^2 \quad (27)$$

Here, the experimental uncertainty of $\Delta(\Delta\nu_C)$ is expressed in a similar fashion to the uncertainty in $\Delta A_{i,C}$ as outlined in Sect. A.2:

$$(\Delta(\Delta\nu_C))^2 = (\Delta\nu_{C,\text{fit}})^2 + (\Delta\nu_{C,C})^2 + (\Delta\nu_{C,J''})^2 \quad (28)$$

Here, $\Delta(\Delta\nu_{C,\text{fit}})$ is the 1-σ standard deviation for the parameter estimate $\Delta(\Delta\nu_C)$ of the spectral fit, $\Delta(\Delta\nu_{C,C})$ is the variation of collision width from the linestrength uncertainty of the P(3,14) line, and $\Delta(\Delta\nu_{C,J''})$ is the uncertainty due to the assumption that the collision width is the same for the three transitions. As seen in Fig. 18, in this work, $\Delta(\Delta\nu_C)$ contributes a smaller amount to the overall uncertainty in P_{tot} compared to $\Delta\gamma_{\text{CO}-\text{mix}}(T)$.

A generalized derivation of the temperature-dependent mixture-weighted collisional broadening coefficient uncertainty $\Delta\gamma_{\text{CO}-\text{mix}}(T)$ is provided in the following subsection. Fig. 19 shows that $\Delta P_{\text{tot}}/P_{\text{tot}}$ has a slight inverse trend over the range of P_{tot} measured in this work; this is largely due to the relatively constant values of $\Delta\gamma_{\text{CO}-\text{mix}}(T)$ combined with the lower values of $\Delta(\Delta\nu_C)$ at higher pressures owing to increased SNR.

Broadening coefficient uncertainty

The uncertainty in the mixture-weighted broadening coefficient $\Delta\gamma_{j-\text{mix}}(T)$ for species j is given by:

$$(\Delta\gamma_{j-\text{mix}}(T))^2$$
$$= \sum_Y \left[(\gamma_{j-Y}(T)\Delta X_Y)^2 + (X_Y\Delta\gamma_{j-Y}(T))^2\right] \quad (29)$$

The mole fractions of the collision partners X_Y are estimated from CJ simulations, so there is a numerically-determined

uncertainty ΔX_Y for each collision partner Y associated with both the uncertainty in local equivalence ratio $\Delta\phi$ and the variation of mole fraction with the assumption of either frozen or equilibrium flow $\Delta X_{Y,\text{FE}}$, as shown in Fig. 6. This is expressed as:

$$\Delta X_Y^2 = \left(\frac{\partial X_Y}{\partial\phi}\Delta\phi\right)^2 + \Delta X_{Y,\text{FE}}^2 \quad (30)$$

We can see from Eq. 29 that uncertainties associated with the major collision partners will be weighted more heavily than those associated with trace collision partners.

The temperature-dependent collisional broadening coefficient $\gamma_{j-Y}(T)$ for species j is modeled according to Eq. 10 for the collision partners CO_2, H_2O, O_2, H_2, and N_2. The uncertainty can be calculated for the collision pairs as:

$$\left(\frac{\Delta\gamma_{j-Y}(T)}{\gamma_{j-Y}(T)}\right)^2 = \left(\frac{\Delta\gamma_{j-Y}(T_0)}{\gamma_{j-Y}(T_0)}\right)^2 + N_{j-Y}^2\left(\frac{\Delta T}{T}\right)^2 + \left(\ln(T_0/T)\Delta N_{j-Y}\right)^2 \quad (31)$$

The uncertainties in reference temperature collisional broadening coefficient $\Delta\gamma_{j-Y}(T_0)$, and temperature-dependent exponent ΔN_{j-Y}, are driven largely by variation with rotational quantum number [53]. For the collision partners OH, H, and O, the uncertainty is calculated as follows:

$$\left(\frac{\Delta\gamma_{j-Y}(T)}{\gamma_{j-Y}(T)}\right)^2 = \left(\frac{\Delta\gamma_{j-\text{N}_2}(T)}{\gamma_{j-\text{N}_2}(T)}\right)^2 + \left(\frac{2\Delta\sigma_{j-Y}}{\sigma_{j-Y}}\right)^2 + \left(\frac{2\Delta\sigma_{j-\text{N}_2}}{\sigma_{j-\text{N}_2}}\right)^2 + \varepsilon_{\text{scale}}^2 \quad (32)$$

To account for uncertainty associated with the scaling assumptions invoked in Eq. 11, the uncertainty dependencies on optical collision diameters σ are also included. $\Delta\sigma$ for CO, N_2, CO_2, are estimated based on experimental uncertainty in virial coefficient data for these species [55], while $\Delta\sigma$ for OH, O, and H are estimated based on variations in the predictions of molecular dynamic simulations [49]. $\varepsilon_{\text{scale}}$ is the error associated with the scaling assumption, obtained by comparing the results of the scaling procedure for j-O_2 with the literature values that are actually utilized for this collision partner, which were on the order of 5%.

Overall, uncertainties in mixture composition, ΔX_Y, contribute more to $\Delta\gamma_{j-\text{mix}}(T)$ than uncertainties in species-specific broadening coefficients, $\Delta\gamma_{j-Y}(T)$, as seen in Fig. 21. We can examine the contributors to $\Delta\gamma_{j-\text{mix}}(T)$ by looking at each species individually, as in Fig. 22.

For both CO and CO_2 measurements, we observe that uncertainties associated with both the mole fraction and the broadening coefficient of H_2O are the most significant contributors by far to the overall uncertainties in broadening
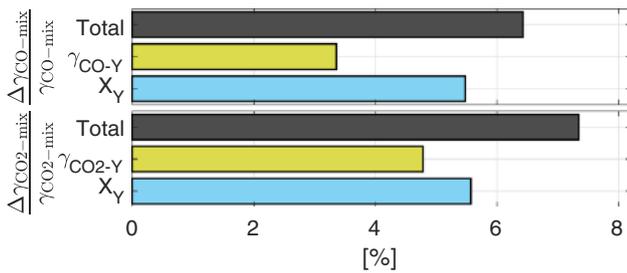
Fig. 21 Averaged representative uncertainty analysis for the mixture-weighted broadening coefficients for CO and CO_2 performed on the test shown in Fig. 16
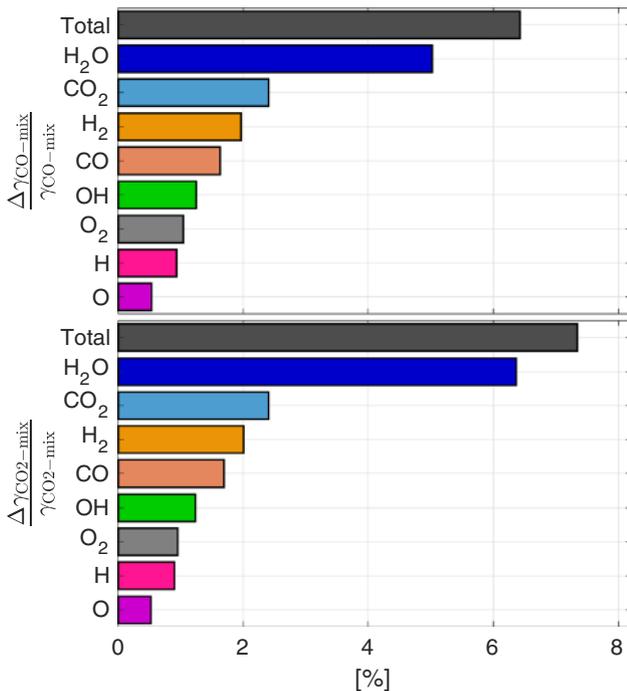
Fig. 22 Averaged representative uncertainty analysis for the mixture-weighted broadening coefficients for CO and CO_2 performed on the test shown in Fig. 16

coefficient, followed by those of CO_2 and H_2, owing to their magnitude. Reducing the uncertainty of either ΔX_Y or $\Delta\gamma_{j-Y}(T)$ —either by measuring additional species or through additional fundamental spectroscopy investigations at high temperatures—represents an opportunity for future research.

Number column density uncertainty

For CO, the experimental uncertainty in number column density can be determined by applying Eq. 19–7:

$$\left(\frac{\Delta N_{CO}}{N_{CO}}\right)^2 = \left(\frac{\Delta S_A(T)}{S_A(T)}\right)^2 + \left(\frac{\Delta A_A}{A_A}\right)^2 \tag{33}$$

$\Delta S_A(T)$ is determined from Eq. 20 through Eq. 21 (Described in Sect. A.1) in which the value of experimental ΔT used in those equations is determined using Eq. 23, while ΔA_A is determined from Eq. 25. In this work, the contributions to overall uncertainty for N_{CO} by $\Delta S_A(T)$ and ΔA_A are similar in magnitude, as shown in Fig. 18. A slight inverse trend is noted when plotting $\Delta N_{CO}/N_{CO}$ vs. N_{CO}, as shown in Fig. 19; overall measurement uncertainty is typically lower as SNR increases with increasing CO density.

For CO_2, the experimental uncertainty in number column density is less straightforward since N_{CO_2} is inferred directly as a free parameter of a nonlinear least-squares fit. Although there is some uncertainty associated with the 1-σ standard deviation for the parameter estimate in the spectral fit, $\Delta N_{CO_2,fit}$, this does not account for uncertainty associated with temperature, pressure, and the collisional broadening coefficients used in the line-mixing model. The dependence of ΔN_{CO_2} on ΔT, ΔP_{tot}, and $\Delta\gamma_{CO_2-Y}(T)$ is determined by numerical application of Eq. 19 to the CO_2 line-mixing model. The assumed T, P, and $\gamma_{CO_2-Y}(T)$ inputs are varied by their respective experimental uncertainties, and the resulting ranges of N_{CO_2} are used to infer ΔN_{CO_2}.

$$\begin{aligned}\left(\Delta N_{CO_2}\right)^2 = &\left(\Delta N_{CO_2,fit}\right)^2 \\ &+ \left(\Delta N_{CO_2,\Delta T}\right)^2 + \left(\Delta N_{CO_2,\Delta P_{tot}}\right)^2 \\ &+ \sum_Y \left(\Delta N_{CO_2,\Delta\gamma_{CO_2-Y}(T)}\right)^2\end{aligned} \tag{34}$$

The most significant influence in the uncertainty for N_{CO_2} are observed to be $\Delta N_{CO_2,fit}$, largely owing to low SNR, followed by ΔT, ΔP_{tot}, and $\Delta\gamma_{CO_2-Y}(T)$, as seen in Fig. 18. This is consistent with the sensitivity of the line-mixing model to collision-induced broadening and rovibrational energy transfers, which depend heavily on T, P_{tot}, and $\gamma_{CO_2-Y}(T)$.

Unquantified uncertainties

The above uncertainty analysis rigorously accounts for most theoretical and practical contributions to measurement uncertainty that are intrinsic to the technique. However, some extrinsic elements of uncertainty that are environment- and hardware-specific are not quantified here, including beam size, alignment, and steering, detector non-linearity, plume expansion, and fringe etalons. The technique has been designed to minimize most of these effects, and their influences are expected to be within the bounds of uncertainty as calculated in this section.

References

1. W.H. Heiser, D.T. Pratt, Thermodynamic cycle analysis of pulse detonation engines. J. Prop. Power **18**(1), 68–76 (2008). https://doi.org/10.2514/2.5899

2. B.R. Bigler, E.J. Paulson, W.A. Hargus, Idealized efficiency calculations for rotating detonation engine rocket applications. in *53rd AIAA/SAE/ASEE J. Prop. Conf.*, 2017. https://doi.org/10.2514/6.2017-5011

3. Y. Zel'dovich, To the question of energy use of detonation combustion. J. Prop. Power **22**(3), 588–592 (2006). https://doi.org/10.2514/1.22705

4. F.K. Lu, E.M. Braun, Rotating detonation wave propulsion: experimental challenges, modeling, and engine concepts. J. Prop. Power **30**(5), 1125–1142 (2014). https://doi.org/10.2514/1.b34802

5. F.A. Bykovskii, S.A. Zhdan, E.F. Vedernikov, Continuous spin detonations. J. Prop. Power **22**(6), 1204–1216 (2006). https://doi.org/10.2514/1.17656

6. P. Wolański, Detonation engines. J KONES Powertrain Trans. **18**(3), 515–521 (2011)

7. R.D. Smith, S. Stanley, Experimental Investigation of Continuous Detonation Rocket Engines for In-Space Propulsion. in *52nd AIAA/SAE/ASEE J. Prop. Conf.*, 2016. https://doi.org/10.2514/6.2016-4582

8. M.L. Fotia, F. Schauer, T. Kaemming, J. Hoke, Experimental study of the performance of a rotating detonation engine with nozzle. J. Prop. Power **32**(3), 674–681 (2016). https://doi.org/10.2514/1.B35913

9. R. Zhou, D. Wu, J. Wang, Progress of continuously rotating detonation engines. Chin. J. Aeronaut. **29**(1), 15–29 (2016). https://doi.org/10.1016/j.cja.2015.12.006

10. B.A. Rankin, M.L. Fotia, A.G. Naples, C.A. Stevens, J.L. Hoke, T.A. Kaemming, S.W. Theuerkauf, F.R. Schauer, Overview of performance, application, and analysis of rotating detonation engine technologies. J. Prop. Power **33**(1), 131–143 (2017). https://doi.org/10.2514/1.B36303

11. W.A. Hargus, S.A. Schumaker, E.J. Paulson, Air Force Research Laboratory Rotating Detonation Rocket Engine Development, in *54th J. Prop. Conf.*, 2018. https://doi.org/10.2514/6.2018-4876

12. J.W. Bennewitz, B.R. Bigler, W.A. Hargus, S.A. Danczyk, R.D. Smith, Characterization of detonation wave propagation in a rotating detonation rocket engine using direct high-speed imaging, in *54th J. Prop. Conf.*, 2018. https://doi.org/10.2514/6.2018-4688

13. C.A. Nordeen, D. Schwer, F. Schauer, J. Hoke, T. Barber, B.M. Cetegen, Role of inlet reactant mixedness on the thermodynamic performance of a rotating detonation engine. Shock Waves **26**(4), 417–428 (2016). https://doi.org/10.1007/s00193-015-0570-7

14. S.M. Frolov, V.A. Smetanyuk, V.S. Ivanov, B. Basara, The influence of the method of supplying fuel components on the characteristics of a rotating detonation Engine. Combustion Sci. Technol. (2019). https://doi.org/10.1080/00102202.2019.1662408

15. W.S. Anderson, S.D. Heister, Response of a liquid jet in a multiple detonation driven crossflow. J.Prop. Power **35**(2), 303–312 (2019). https://doi.org/10.2514/1.B37127

16. W. Anderson, S.D. Heister, C. Hartsfield, Experimental study of a hypergolically ignited liquid bipropellant rotating detonation rocket engine, in *2019 AIAA Scitech Forum*, 2019. https://doi.org/10.2514/6.2019-0474

17. W.Y. Peng, S.J. Cassady, C.L. Strand, C.S. Goldenstein, R.M. Spearrin, C.M. Brophy, J.B. Jeffries, R.K. Hanson, Single-ended mid-infrared laser-absorption sensor for time-resolved measurements of water concentration and temperature within the annulus of a rotating detonation engine. Proc. Combustion Inst. **37**(2), 1435–1443 (2019). https://doi.org/10.1016/j.proci.2018.05.021

18. C.S. Goldenstein, R.M. Spearrin, J.B. Jeffries, R.K. Hanson, Infrared laser absorption sensors for multiple performance parameters in a detonation combustor. Proc. Combustion Inst. **35**(3), 3739–3747 (2015). https://doi.org/10.1016/j.proci.2014.05.027

19. R.M. Spearrin, C.S. Goldenstein, J.B. Jeffries, R.K. Hanson, Quantum cascade laser absorption sensor for carbon monoxide in high-pressure gases using wavelength modulation spectroscopy.

20. R.M. Spearrin, C.S. Goldenstein, J.B. Jeffries, R.K. Hanson, Mid-infrared laser absorption diagnostics for detonation studies, in *29th International Symposium on Shock Waves 1*, (Springer International Publishing, Cham, 2015), pp. 259–264. https://doi.org/10.1007/978-3-319-16835-7_39

21. S.T. Sanders, J.A. Baldwin, T.P. Jenkins, D.S. Baer, R.K. Hanson, Diode-laser sensor for monitoring multiple combustion parameters in pulse detonation engines. Proc. Combustion Inst. **28**(1), 587–594 (2000). https://doi.org/10.1016/s0082-0784(00)80258-1

22. A.W. Caswell, S. Roy, X. An, S.T. Sanders, F.R. Schauer, J.R. Gord, Measurements of multiple gas parameters in a pulsed-detonation combustor using timedivision-multiplexed Fourier-domain mode-locked lasers. Appl. Opt. **52**(12), 2893–2904 (2013). https://doi.org/10.1364/AO.52.002893

23. L. Ma, S.T. Sanders, J.B. Jeffries, R.K. Hanson, Monitoring and control of a pulse detonation engine using a diode-laser fuel concentration and temperature sensor. Proc. Combustion Inst. **29**(1), 161–166 (2002). https://doi.org/10.1016/S1540-7489(02)80025-6

24. A.E. Klingbeil, J.B. Jeffries, R.K. Hanson, Design of a fiber-coupled mid-infrared fuel sensor for pulse detonation engines. AIAA J. **45**(4), 772–778 (2007). https://doi.org/10.2514/1.26504

25. D.D. Lee, F.A. Bendana, S.A. Schumaker, R.M. Spearrin, Wavelength modulation spectroscopy near 5 μm for carbon monoxide sensing in a high-pressure kerosene-fueled liquid rocket combustor. Appl. Phys. B **124**(5), 77 (2018). https://doi.org/10.1007/s00340-018-6945-6

26. C.S. Goldenstein, C.A. Almodóvar, J.B. Jeffries, R.K. Hanson, C.M. Brophy, High-bandwidth scanned-wavelength-modulation spectroscopy sensors for temperature and H_2O in a rotating detonation engine. Measurement Science and Technology **25**(10), 105–104 (2014). https://doi.org/10.1088/0957-0233/25/10/105104

27. S.J. Cassady, W.Y. Peng, C.L. Strand, J.B. Jeffries, R.K. Hanson, D.F. Dausen, C.M. Brophy, A single-ended, mid-IR sensor for time-resolved temperature and species measurements in a hydrogen/ethylene-fueled rotating detonation engine, in *2019 AIAA Scitech 2019 Forum*, 2019. https://doi.org/10.2514/6.2019-0027

28. K.D. Rein, S. Roy, S.T. Sanders, A.W. Caswell, F.R. Schauer, J.R. Gord, Measurements of gas temperatures at 100 kHz within the annulus of a rotating detonation engine. Appl. Phys. B **123**(3), 88 (2017). https://doi.org/10.1007/s00340-017-6647-5

29. Arroyo Instruments (2015) 6300 Series ComboSource User's Manual. https://www.arroyoinstruments.com/product-lines/6300

30. M. Raza, L. Ma, C. Yao, M. Yang, Z. Wang, Q. Wang, R. Kan, W. Ren, MHz-rate scanned-wavelength direct absorption spectroscopy using a distributed feedback diode laser at 2.3 μm. Optics & Laser Technology **130**(May), 106344 (2020). https://doi.org/10.1016/j.optlastec.2020.106344

31. G.C. Mathews, C.S. Goldenstein, Wavelength-modulation spectroscopy for MHz thermometry and H_2O sensing in combustion gases of energetic materials, in *2019 AIAA Scitech Forum*, 2019. https://doi.org/10.2514/6.2019-1609

32. B. Hinkov, A. Hugi, M. Beck, J. Faist, Rf-modulation of mid-infrared distributed feedback quantum cascade lasers. Opt. Express **24**(4), 3294 (2016). https://doi.org/10.1364/oe.24.003294

33. R.S. Chrystie, E.F. Nasir, A. Farooq, Towards simultaneous calibration-free and ultra-fast sensing of temperature and species in the intrapulse mode. Proc. Combustion Inst. **35**(3), 3757–3764 (2015). https://doi.org/10.1016/j.proci.2014.06.069

34. R.M. Spearrin, S. Li, D.F. Davidson, J.B. Jeffries, R.K. Hanson, High-temperature iso-butene absorption diagnostic for shock tube kinetics using a pulsed quantum cascade laser near 11.3 μm. Proc. Combustion Inst **35**(3), 3645–3651 (2015). https://doi.org/10.1016/j.proci.2014.04.002. http://linkinghub.elsevier.com/retrieve/pii/S1540748914000030

35. D.I. Pineda, F.A. Bendana, K.K. Schwarm, R.M. Spearrin, Multi-isotopologue laser absorption spectroscopy of carbon monoxide for high-temperature chemical kinetic studies of fuel mixtures. Combustion Flame **207**, 379–390 (2019). https://doi.org/10.1016/j.combustflame.2019.05.030

36. R.K. Hanson, M.R. Spearrin, C.S. Goldenstein, Spectroscopy and Optical Diagnostics for Gases. (2016). https://doi.org/10.1007/978-3-319-23252-2

37. C.S. Goldenstein, I.A. Schultz, J.B. Jeffries, R.K. Hanson, Two-color absorption spectroscopy strategy for measuring the column density and path average temperature of the absorbing species in nonuniform gases. Appl. Opt. **52**(33), 7950–7962 (2013). https://doi.org/10.1364/AO.52.007950

38. L. Rothman, I. Gordon, R. Barber, H. Dothe, R. Gamache, A. Goldman, V. Perevalov, S. Tashkun, J. Tennyson, HITEMP, the high-temperature molecular spectroscopic database. J. Quantitative Spectrosc. Radiat. Trans. **111**(15), 2139–2150 (2010). https://doi.org/10.1016/j.jqsrt.2010.05.001

39. F.A. Bendana, D.D. Lee, C. Wei, D.I. Pineda, R.M. Spearrin, Line mixing and broadening in the $v(1 \rightarrow 3)$ first overtone bandhead of carbon monoxide at high temperatures and high pressures. J. Quantitative Spectrosc. Radiat. Trans. **239**, 106636 (2019). https://doi.org/10.1016/j.jqsrt.2019.106636

40. C.S. Goldenstein, R.M. Spearrin, J.B. Jeffries, R.K. Hanson, Infrared laser-absorption sensing for combustion gases. Progress Energy Combustion Sci. **60**, 132–176 (2017). https://doi.org/10.1016/j.pecs.2016.12.002

41. A.B. McLean, C.E. Mitchell, D.M. Swanston, Implementation of an efficient analytical approximation to the Voigt function for photoemission lineshape analysis. J. Electron Spectrosc. Related Phenomena **69**(2), 125–132 (1994). https://doi.org/10.1016/0368-2048(94)02189-7

42. J.M. Hartmann, L. Rosenmann, M.Y. Perrin, J. Taine, Accurate calculated tabulations of CO line broadening by H_2O, N_2, O_2, and CO_2 in the 200–3000-K temperature range. Appl. Opt. **27**(15), 3063 (1988). https://doi.org/10.1364/ao.27.003063

43. S. Browne, J. Ziegler, J.E. Shepherd, numerical solution methods for shock and detonation jump conditions. GALCIT Report FM2006006 (July 2004) (2008)

44. D.G. Goodwin, H.K. Moffat, R.L. Speth, Cantera: An object-oriented software toolkit for chemical kinetics, thermodynamics, and transport processes. (2018). https://doi.org/10.5281/zenodo.170284

45. G.P. Smith, D.M. Golden, M. Frenklach, N.W. Moriarty, B. Eiteneer, M. Goldenberg, C.T. Bowman, R.K. Hanson, S. Song, W.C. Gardiner, V.V. Lissianski, Z. Qin, GRI-MECH 3.0 (1999). http://www.me.berkeley.edu/gri_mech/

46. R. Sur, K. Sun, J.B. Jeffries, R.K. Hanson, Multi-species laser absorption sensors for in situ monitoring of syngas composition. Appl. Phys. B **115**(1), 9–24 (2014). https://doi.org/10.1007/s00340-013-5567-2

47. S. Sandler, J. Wheatley, Intermolecular potential parameter combining rules for the Lennard-Jones 6–12 potential. Chemical Physics Letters **10**(4), 375–378 (1971). https://doi.org/10.1016/0009-2614(71)80313-5

48. D.R. Eaton, F.R.S. Thompson, Pressure broadening studies on vibration-rotation bands II. The effective collision diameters. Proc. R. Soc. Lond. Ser. A Math. Phys. Sci. **251**(1267), 475–485 (1959). https://doi.org/10.1098/rspa.1959.0120

49. A.W. Jasper, J.A. Miller, Lennard–Jones parameters for combustion and chemical kinetics modeling from full-dimensional intermolecular potentials. Combustion Flame **161**(1), 101–110 (2014). https://doi.org/10.1016/j.combustflame.2013.08.004

50. J.M. Hartmann, C. Boulet, D. Robert, *Collisional effects on molecular spectra* (Elsevier, 2008). https://doi.org/10.1016/B978-0-444-52017-3.X0001-5

51. F.A. Bendana, D.D. Lee, S.A. Schumaker, S.A. Danczyk, R.M. Spearrin, Cross-band infrared laser absorption of carbon monoxide for thermometry and species sensing in high-pressure rocket flows. Appl. Phys. B **125**(11), 204 (2019). https://doi.org/10.1007/s00340-019-7320-y

52. D.D. Lee, F.A. Bendana, A.P. Nair, D.I. Pineda, R.M. Spearrin, Line mixing and broadening of carbon dioxide by argon in the v_3 bandhead near 4.2 μm at high temperatures and high pressures. J. Quantitative Spectrosc. Radiat. Trans. 107135 (2020). https://doi.org/10.1016/j.jqsrt.2020.107135

53. L. Rosenmann, J.M. Hartmann, M.Y. Perrin, J. Taine, Accurate calculated tabulations of IR and Raman CO2 line broadening by CO_2, H_2O, N_2, O_2 in the 300–2400-K temperature range. Appl. Opt. **27**(18), 3902 (1988). https://doi.org/10.1364/AO.27.003902

54. H.W. Coleman, W.G. Steele, *Experimentation, validation, and uncertainty analysis for engineers*, 3rd edn. (Wiley, Hoboken, 2009)

55. D.I. Pineda, T.A. Casey, Virial Coefficient Data for Combustion Species. GitHub (2017). https://doi.org/10.5281/zenodo.852698. https://github.com/Combustion-Transport-Analysis/Virial-Coefficient-Data-for-Combustion-Species

Publisher's Note Springer Nature remains neutral with regard to jurisdictional claims in published maps and institutional affiliations.